Hindawi
Structural Control and Health Monitoring
Volume 2023, Article ID 4170149, 21 pages
https://doi.org/10.1155/2023/4170149

Research Article

Time-Domain Finite Element Model Updating for Operational Monitoring and Damage Identification of Bridges

Niloofar Malekghaini,[1] Farid Ghahari,[2] Hamed Ebrahimian,[1] Matthew Bowers,[3] Hoda Azari,[4] and Ertugrul Taciroglu[2]

[1]*Department of Civil and Environmental Engineering, University of Nevada, Reno, NV, USA*
[2]*Department of Civil and Environmental Engineering, University of California, Los Angeles, CA, USA*
[3]*SC Solutions Inc, Sunnyvale, CA, USA*
[4]*Federal Highway Administration, McLean, VA, USA*

Correspondence should be addressed to Hamed Ebrahimian; hebrahimian@unr.edu

Received 3 October 2022; Accepted 7 April 2023; Published 31 July 2023

Academic Editor: Lucia Faravelli

The well-known limitations of modal system identification methods have led to a broad exploration of alternative solutions for operational monitoring and damage diagnosis of structures. This study presents a time-domain Bayesian finite element model updating approach to jointly identify the vehicular loads and finite element modeling parameters of bridges using the vibration data and the location of vehicles traversing the bridge as input. A Bayesian model updating is devised and verified through a series of case studies based on numerically simulated data from a prestressed reinforced concrete box-girder bridge model. Damage states are defined for concrete degradation and delamination, steel corrosion, and loss of prestressing force. Ten different damage scenarios, encompassing the range from minor localized to major distributed damage, are examined. The responses of the damaged bridge are simulated under random traffic scenarios. The acceleration responses, along with the location of the vehicles on the bridge, are used for jointly estimating the model parameters and vehicular loads. The estimated model parameters are then used to infer the location and extent of damage within the bridge. The results show the successful performance of the proposed approach in a numerically simulated environment.

1. Introduction

America's bridges, which are a critical element of its transportation infrastructure, are aging and decaying. There are more than 600,000 bridges across the U.S., nearly 40% of which are 50 years or older. In 2016, one in 11 bridges was identified as being structurally deficient while collectively serving 188 million daily trips [1]. Replacement or rehabilitation of such a large number of bridges is a monumental task, possibly requiring decades to complete. Consequently, structurally deficient and obsolete bridges will remain in service for extended time periods. To ensure public safety, it is necessary to examine solutions for operational monitoring of bridges—a capability that could provide actionable quantitative information to guide decision-making.

Visual inspection is the most common approach to monitor the condition of structural members in bridges. In this approach, the damage is identifiable only when it is visually apparent, which may leave important damage mechanisms undiscovered until catastrophic failure [2]. Visual inspection is costly, labor-intensive, and inherently subjective. The damage assessment through this approach is generally qualitative and may not yield critical insights into the overall condition of the inspected bridge [3, 4]. Hence, there is a need to develop cost-effective solutions to detect, localize, and quantify various damage types and evaluate their effects on the load-bearing capacity and structural safety.

Nondestructive evaluation (NDE) is perhaps the most accurate technique for localized damage identification and condition assessment of bridges [2]. Through NDE techniques, numerous subsurface damage mechanisms, including concrete delamination, steel corrosion, and fracture in prestressing wires, etc., can be quantitatively evaluated for accessible structural members/components. Nevertheless, NDE techniques require well-trained and experienced personnel for the data collection, processing, and interpretation [5–7]. These techniques are costly and often require traffic interruptions. Considering the fact that there are approximately 390 million square meters of bridge decks in the U.S. that need to be inspected, relying only on NDE techniques can lead to an onerous undertaking [8]. Therefore, there is a need to introduce complementary screening methods to detect, localize, and quantify damage in bridge members in order to guide the targeted application of NDE techniques [9, 10]. The damage identification approach proposed herein can provide a potentially cost-effective solution toward this objective.

Vibration-based monitoring offers another family of approaches that can be used for damage identification. In these approaches, dynamic responses are collected and processed through data-driven or model-based techniques. Data-driven techniques include statistical pattern recognition and machine learning methods to learn from data patterns and detect anomalies [11] or modal system identification methods, which extract natural frequencies or mode shapes (or other derivative information) that are sensitive to damage [12]. These methods can be useful to detect damage as a change in baseline response patterns of the structure [13] but are often ineffective for damage localization and quantification in civil engineering applications due to the typically low spatial density of deployed sensors and generally low signal-to-noise ratio of recordings. Although data-driven techniques remove the burden of devising models, they lack the capacity to incorporate and leverage the mechanics-based knowledge of structural behavior into the damage identification process. Model-based techniques most often include a mode-based linear finite element (FE) model updating approach, in which the identified modal properties of the structure are used to estimate the parameters of a linear FE model. Once determined, the estimated model parameters can be used for inferring structural damage [14]. The application of linear FE model updating methods has not been traditionally successful for damage identification of bridges under operational conditions. The main reason is that modal properties are not generally sensitive to typical aging- and degradation-related damage types in bridges [12]. Such damage is typically observable only through the structure's higher modes, the identification of which can be difficult. Furthermore, the underlying assumptions in modal identification are often violated in the operational monitoring of bridges. Specifically, the broadband stationary excitation assumption is often not realized under traffic loading, which requires more advanced modal identification techniques [15–17]. Moreover, the linear-elastic behavior assumption can often be violated, especially for reinforced concrete bridges [18, 19].

To circumvent the shortcomings of modal FE model updating methods, time-domain FE model updating has gained attention in the literature. This technique can be developed using optimization or stochastic filtering approaches. In optimization-based methods, the model parameters are estimated to minimize the discrepancy between measured and FE-predicted responses [20]. These methods are often less stable and computationally more demanding than stochastic filtering methods, which allow the consideration of uncertainties in the model updating process and enable the uncertainty quantification of the estimated model and the input parameters [21]. The FE model updating using Bayesian filters, including extended Kalman filter (EKF) and unscented Kalman filter (UKF), have been used for structural engineering applications [22–25]. The Bayesian FE model updating approaches are developed to estimate the input [26, 27] or input and states of structural systems [28, 29]. Damage identification through the FE model updating approach requires the estimation of mechanics-based model parameters (e.g., material properties). Deviation of the updated model parameters from their nominal values can reveal information about the location and extent of damage in the structure [30].

This study proposes extending the Bayesian FE model updating techniques to bridges under traffic loads for operational monitoring and damage identification. While the Bayesian FE model updating techniques have already been developed for model-only or joint-input-model identification problems based on earthquake loads [21, 31–35] or wind loads [36], prior applications are fundamentally different from the current problem, wherein moving (traffic) loads are the input to the system. Earthquake and wind load inputs are characterized by unknown time-histories applied at known locations, while traffic loads constitute unknown, discrete, and continuously moving vehicular loads. These differences in the problem statement require a novel Bayesian model updating formulation. In the present study, the tracked locations of vehicles traversing the bridge, which are synchronized with the recorded vibration responses of the bridge, are used for the joint estimation of the FE model parameters and vehicular loads. The estimated FE model parameters can be used to infer the location, mechanism, and extent of damage in different regions of the bridge, with the premise that the relatively large excitations induced by vehicular loads are adequate to illuminate changes in structural parameters due to damage.

In what follows, the aforementioned novel Bayesian FE model updating formulation is presented (§2 and §3) and verified using synthetic yet realistic data generated through detailed simulations with a prestressed concrete box-girder bridge model featuring ten different types of damages (§4 and §5). Various conclusions are also provided at the end (§6).

2. Proposed Approach for Bridge Operational Monitoring and Damage Identification

As shown in Figure 1, in the present approach, the class and location of vehicles traversing the bridge are obtained from traffic cameras using a computer vision technique. The

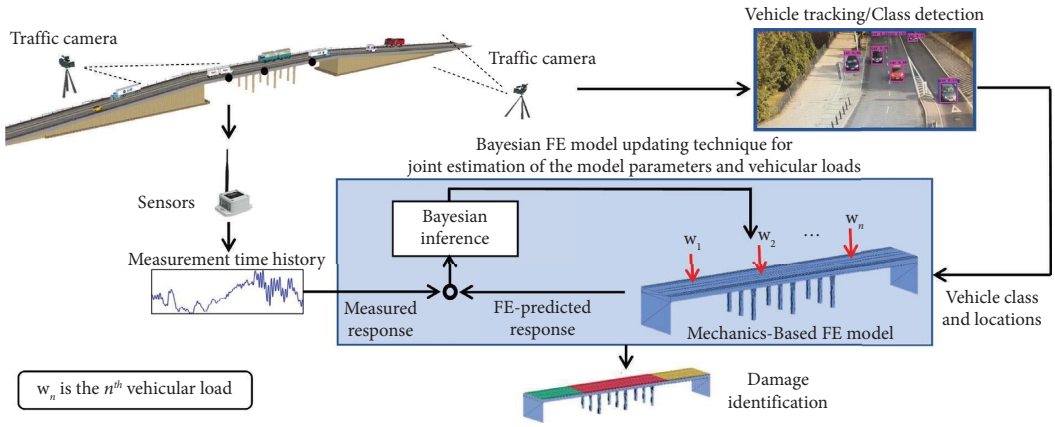

FIGURE 1: The proposed approach for operational monitoring and damage identification of bridges by integrating mechanics-based FE models with data obtained from vibration sensors and traffic cameras.

dynamic responses of the bridge due to the traffic load are assumed to be measured using a variety of sensors (e.g., accelerometers and noncontact displacement sensors). The class and location time-history data for the vehicles and the measured dynamic responses of the bridge are then used as inputs to a Bayesian FE model updating technique, the establishment of which is the focal point of the present study and will be discussed in the next section.

Although the adopted computer vision technique to track the vehicles on the bridge and identify their classes (e.g., car, truck, and bus) and locations from camera recordings is not the subject of this study, some details are provided here for the benefit of the reader, and further details can be found in [37, 38]. The overall technique is based on a track-by-detection scheme. The detector is based on the "You Only Look Once version 3 (YOLOv3)" algorithm [39], and the tracker is based on the Deep-SORT [40] technique, which uses the motion and appearance characteristics of the detected vehicles. The identified tracks are transformed from the image coordinate system to the physical bridge deck coordinate system, which is achieved by using markers in the camera view with known positions.

Through the Bayesian FE model updating process, the unknown parameters characterizing the mechanical properties of the model along with the vehicular loads are estimated. These parameters are treated as random variables, the uncertainties of which are characterized by a joint probability density function (PDF). Through a Bayesian inference, the information contained in the measured data is used to update the prior PDF to yield the most probable estimates. The updated model with quantified uncertainties can be regarded as a digital twin of the real-world asset, which can be utilized for various applications including load rating and asset management throughout the lifetime of the bridge.

3. Bayesian Finite Element Model Updating Technique for Joint Estimation of Model Parameters and Vehicular Loads

The FE model updating techniques for joint estimation of model parameters and input have been developed previously based on extended Kalman filters [21] and dual Kalman filters [29]. These methods have been used for output-only system identification of structures under seismic excitations (e.g., [21, 28, 34, 41]). The Bayesian FE model updating formulation proposed in this paper is relatively similar to the works presented in [21, 29] and is extended to apply for the joint model parameter and vehicular load estimation problem herein.

The response of the FE model of a bridge structure at time step t to a set of vehicular loads with known position time history can be expressed as a nonlinear function of the model parameter vector, $\boldsymbol{\theta} \in \mathbb{R}^{n_{\boldsymbol{\theta}} \times 1}$, the vehicular load vector for the vehicles that enter the bridge between time step $t_0 = 1$ and time step t, $\mathbf{w}_t \in \mathbb{R}^{n_{\mathbf{w},t} \times 1}$, and the initial condition of the dynamic states of the bridge, $\mathbf{x}_0$, as follows:

$$\hat{\mathbf{y}}_t = \mathbf{h}_t(\boldsymbol{\theta}, \mathbf{w}_t, \mathbf{x}_0), \tag{1}$$

where $\hat{\mathbf{y}}_t \in \mathbb{R}^{n_y \times 1}$ is the FE-predicted response of the bridge and $\mathbf{h}_t(\ldots)$ is the nonlinear response function of the FE model at time step t, encapsulating the dynamics of the model from time step $t_0 = 1$ to t. The term $n_{\boldsymbol{\theta}}$ is the number of model parameters, $n_{\mathbf{w},t}$ is the number of vehicles that enter the bridge from time step t_0 to time step t, and $n_{\mathbf{y}}$ is the number of measurement channels. In this study, we assume an at-rest initial condition, i.e., $\mathbf{x}_0 = \mathbf{0}$. Due to this assumption, the term $\mathbf{x}_0$ is excluded from the rest of the formulations. However, at-rest initial condition may be difficult to achieve in real-world applications and addressing this can be the subject of future validation studies.

The response of the bridge under traffic excitation is measured using a set of sensors. The simulation error vector at time step t is defined as $\boldsymbol{\lambda}_t(\boldsymbol{\theta}, \mathbf{w}_t) \in \mathbb{R}^{n_y \times 1}$, which describes the discrepancy between the measured, $\mathbf{y}_t$, and FE-predicted, $\mathbf{h}_t(\boldsymbol{\theta}, \mathbf{w}_t)$, responses of the bridge as follows:

$$\boldsymbol{\lambda}_t(\boldsymbol{\theta}, \mathbf{w}_t) = \mathbf{y}_t - \mathbf{h}_t(\boldsymbol{\theta}, \mathbf{w}_t). \tag{2}$$

The simulation error vector nominally includes the measurement noise and the effects of modeling error [31]. However, the effects of modeling error, including modeling simplification and inaccuracies, uncertainty in geometry and boundary conditions, vehicle location error, and vehicle-

bridge interaction, in this initial verification study are neglected, and the measurement noise is modeled as a stationary and independent (in time and space) zero-mean Gaussian white noise process with the PDF shown in equation (3). It should be noted that this is a somewhat limiting assumption that may be violated in a real-world setting; however, addressing this issue is beyond the scope of present study and is a candidate for future improvements. In equation (3), $\mathbf{R} \in \mathbb{R}^{n_y \times n_y}$ is the diagonal covariance matrix of the simulation error, $|\mathbf{R}|$ denotes its determinant, and superscript T denotes matrix/vector transpose operator.

$$p(\boldsymbol{\lambda}_t) = \frac{1}{(2\pi)^{n_y/2}|\mathbf{R}|^{1/2}} e^{-1/2\boldsymbol{\lambda}_t{}^T \mathbf{R}^{-1}\boldsymbol{\lambda}_t}. \tag{3}$$

A window-based approach is selected to formulate the Bayesian FE model updating technique. In this approach, instead of utilizing the entire batch of the measured data, the time-domain data is divided into a number of windows and the unknown parameters are estimated at each window sequentially. This helps improve the performance and computational efficiency of the model updating process compared to a batch approach [20].

Contrary to previous studies that utilize a series of overlapping sequential windows [21, 34, 36], a rolling estimation window method is devised here to formulate the Bayesian FE model updating technique, as shown schematically in Figure 2. In this method, the time domain is divided into n_s estimation windows and the s^{th} estimation window covers time step $t_0 = 1$ to t_s, i.e., it overlaps with the entire previous window. Therefore, as its name implies, the estimation window *rolls up* in time. This method is developed because the conventional sequential windowing is not applicable to the problem of moving vehicles on the bridge.

Each vehicular load affects the response of the bridge at least for the period of time that the vehicle traverses the bridge. In this initial verification study, at the s^{th} estimation window, the loads of all vehicles that enter the bridge from the beginning (time step t_0) to time step t_s are considered as unknown parameters. The unknown parameters, which are already estimated in the previous windows, will be transferred and re-estimated at the s^{th} estimation window. It is noteworthy that in the standard Kalman filter, the size of state vector is fixed. However, this condition is not maintained in this specific problem as vehicles can enter and exit the bridge at any time with various speeds. Rolling estimation method is a new approach specifically designed and formulated to address this problem.

It is worth noting that the selection of n_s and the length of estimation windows, $(t_s - t_0)\forall s \geq 2$, may depend on the problem configuration (e.g., length of the bridge and number of vehicles) and computational resources, and would be based on the judgment and experience. In general, it is advised to select the rolling rate (i.e., $t_s - t_{s-1}$ for $\forall s \geq 1$) large enough to ensure the presence of at least one vehicle over $[t_{s-1} t_s]$ on the bridge. Moreover, smaller rolling rates reflect more gradual data assimilation, resulting in more stable parameter estimation.

The estimation problem is solved across each estimation window iteratively using all the measured data from time step t_0 to t_s to estimate the model parameters and vehicular loads that enter the bridge across that window. After achieving convergence criteria for a given estimation window, the estimation window is rolled up to include the next batch of data. The statistical properties of the vehicular loads that are common between the new and previous estimation windows are transferred from the previous estimation window to the new one together with the model parameters, and the estimation procedure is repeated in the new window.

The extended estimation parameter vector for the s^{th} estimation window is defined as $\boldsymbol{\varphi}_s = \left[\begin{array}{cc} \boldsymbol{\theta}^T & \mathbf{w}_{t_s}{}^T \end{array}\right]^T$ in which $\mathbf{w}_{t_s}$ is the vector of vehicular loads that are estimated at the s^{th} estimation window-i.e., vehicles that enter the bridge between t_0 to t_s. The Bayes' theorem at the s^{th} estimation window can be applied as follows:

$$p\left(\boldsymbol{\varphi}_s | \mathbf{y}_{1:\,t_s}\right) = \frac{p\left(\mathbf{y}_{1:\,t_s} | \boldsymbol{\varphi}_s\right) \times p(\boldsymbol{\varphi}_s)}{p\left(\mathbf{y}_{1:\,t_s}\right)}. \tag{4}$$

In equation (4), the term $p(\boldsymbol{\varphi}_s | \mathbf{y}_{1:t_s})$ is the joint posterior PDF of the model parameters and vehicular loads and $p(\boldsymbol{\varphi}_s)$ is prior PDF of model parameters and vehicular loads. The term $\mathbf{y}_{1:t_s} = \left[\begin{array}{cccc} \mathbf{y}_1^T & \mathbf{y}_2^T & \cdots & \mathbf{y}_{t_s}^T \end{array}\right]^T$ is the time history of the measured bridge response at the s^{th} estimation window, and $p(\mathbf{y}_{1:t_s} | \boldsymbol{\varphi}_s)$ is the likelihood function. The term $p(\mathbf{y}_{1:t_s})$ is referred to as evidence and is a constant. Following equation (2), $p(\mathbf{y}_{1:t_s} | \boldsymbol{\varphi}_s) = p(\boldsymbol{\lambda}_{1:t_s})$; therefore,

$$p\left(\mathbf{y}_{1:\,t_s} | \boldsymbol{\varphi}_s\right) = \prod_{m=1}^{t_s} \frac{1}{(2\pi)^{n_y/2}|\mathbf{R}|^{1/2}} e^{-1/2\,\left(\mathbf{y}_m - \mathbf{h}_m(\boldsymbol{\theta}, \mathbf{w}_m)\right)^T \mathbf{R}^{-1} \left(\mathbf{y}_m - \mathbf{h}_m(\boldsymbol{\theta}, \mathbf{w}_m)\right)}. \tag{5}$$

In order to jointly estimate the model parameters and vehicular loads, the joint posterior PDF of the model parameters and vehicular loads should be maximized. This can be expressed as follows:

$$\left(\widehat{\boldsymbol{\varphi}}_s\right)_{\text{MAP}} = \underset{(\boldsymbol{\varphi}_s)}{\text{argmax}} \log\left(p\left(\boldsymbol{\varphi}_s \,|\, \mathbf{y}_{1:t_s}\right)\right), \tag{6}$$

where MAP denotes the *maximum a posteriori* estimate. Deriving the natural logarithm from equation (4) results in the following equation:

$$\log\left(p\left(\boldsymbol{\varphi}_s \,|\, \mathbf{y}_{1:t_s}\right)\right) = c_1 + \log\left(p\left(\mathbf{y}_{1:t_s} \,|\, \boldsymbol{\varphi}_s\right)\right) + \log\left(p(\boldsymbol{\varphi}_s)\right), \tag{7}$$

where c_1 is a constant. Substituting equations (5) into (7) and considering a Gaussian distribution for the prior PDF of the extended estimation parameter vector leads to the following equation for the log-posterior PDF:

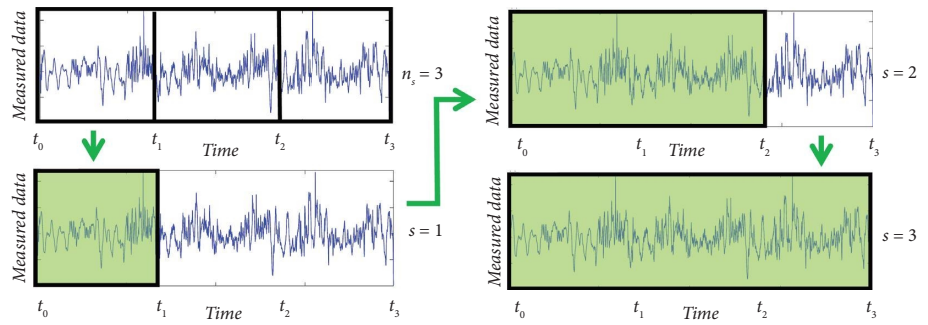

FIGURE 2: Rolling estimation window method for the Bayesian FE model updating technique. The top left figure shows the time history of the measured data. Here the data is divided schematically into three estimation windows and the estimation will be completed sequentially using these three windows.

$$\log\left(p\left(\boldsymbol{\varphi}_s \,|\, \mathbf{y}_{1:t_s}\right)\right) = c_2 - \frac{1}{2}\left(\mathbf{y}_{1:t_s} - \mathbf{h}_{1:t_s}(\boldsymbol{\varphi}_s)\right)^T \tilde{\mathbf{R}}_s^{-1}\left(\mathbf{y}_{1:t_s} - \mathbf{h}_{1:t_s}(\boldsymbol{\varphi}_s)\right) - \frac{1}{2}(\boldsymbol{\varphi}_s - \hat{\boldsymbol{\varphi}}_s^-)^T\left(\hat{\mathbf{P}}_{\boldsymbol{\varphi},s}^-\right)^{-1}(\boldsymbol{\varphi}_s - \hat{\boldsymbol{\varphi}}_s^-), \tag{8}$$

where $\mathbf{h}_{1:t_s} = \left[\mathbf{h}_1^T \;\; \mathbf{h}_2^T \;\; \ldots \;\; \mathbf{h}_{t_s}^T\right]^T$ and c_2 is a constant. The terms $\hat{\boldsymbol{\varphi}}_s^- \in \mathbb{R}^{(n_\theta + n_{w,t_s})\times 1}$ and $\hat{\mathbf{P}}_{\boldsymbol{\varphi},s}^- \in \mathbb{R}^{(n_\theta + n_{w,t_s})\times(n_\theta + n_{w,t_s})}$ are the prior mean vector and prior covariance matrix of the extended estimation parameter vector at the s^{th} estimation window. Considering the definition of vector $\mathbf{y}_{1:t_s} \in \mathbb{R}^{(t_s \times n_y)\times 1}$, the matrix $\tilde{\mathbf{R}}_s \in \mathbb{R}^{(t_s \times n_y)\times(t_s \times n_y)}$ is a block diagonal matrix with the simulation error covariance matrix $\mathbf{R}$ on the diagonal blocks as follows:

$$\tilde{\mathbf{R}}_s = \begin{bmatrix} (\mathbf{R})_{n_y \times n_y} & 0 & \cdots & 0 \\ 0 & (\mathbf{R})_{n_y \times n_y} & \vdots & 0 \\ \vdots & \vdots & \ddots & \vdots \\ 0 & 0 & \cdots & (\mathbf{R})_{n_y \times n_y} \end{bmatrix}_{(t_s \times n_y)\times(t_s \times n_y)}. \tag{9}$$

The posterior joint PDF in equation (8) is maximized by setting $\partial \log(p(\boldsymbol{\varphi}_s|\mathbf{y}_{1:t_s}))/\partial \boldsymbol{\varphi}_s = 0$, which can be solved as

$$\left(\frac{\partial \mathbf{h}_{1:t_s}(\boldsymbol{\varphi}_s)}{\partial \boldsymbol{\varphi}_s}\right)^T \tilde{\mathbf{R}}_s^{-1}\left(\mathbf{y}_{1:t_s} - \mathbf{h}_{1:t_s}(\boldsymbol{\varphi}_s)\right) - \left(\hat{\mathbf{P}}_{\boldsymbol{\varphi},s}^-\right)^{-1}(\boldsymbol{\varphi}_s - \hat{\boldsymbol{\varphi}}_s^-) = \mathbf{0}, \tag{10}$$

and a first-order approximation of $\mathbf{h}_{1:t_s}(\boldsymbol{\varphi}_s)$ can be derived as

$$\mathbf{h}_{1:\,t_s}(\boldsymbol{\varphi}_s) \sim \mathbf{h}_{1:\,t_s}(\hat{\boldsymbol{\varphi}}_s^-) + \left.\frac{\partial \mathbf{h}_{1:\,t_s}(\boldsymbol{\varphi}_s)}{\partial \boldsymbol{\varphi}_s}\right|_{\boldsymbol{\varphi}_s = \hat{\boldsymbol{\varphi}}_s^-}(\boldsymbol{\varphi}_s - \hat{\boldsymbol{\varphi}}_s^-). \tag{11}$$

The term $\partial \mathbf{h}_{1:\,t_s}(\boldsymbol{\varphi}_s)/\partial \boldsymbol{\varphi}_s|_{\boldsymbol{\varphi}_s = \hat{\boldsymbol{\varphi}}_s^-}$ is the FE response sensitivity matrix with respect to the extended estimation parameter vector at $\hat{\boldsymbol{\varphi}}_s^-$ and is denoted by $\mathbf{C} \in \mathbb{R}^{(t_s \times n_y)\times(n_\theta + n_{w,t_s})}$. In this study, the matrix $\mathbf{C}$ is calculated using a finite difference method. Substituting equations (11) into (10) results in the following first-order approximation equation for the MAP estimate of $\boldsymbol{\varphi}_s$:

$$\hat{\boldsymbol{\varphi}}_s^+ = \hat{\boldsymbol{\varphi}}_s^- + \left(\mathbf{C}^T \tilde{\mathbf{R}}_s^{-1}\mathbf{C} + \left(\hat{\mathbf{P}}_{\boldsymbol{\varphi},s}^-\right)^{-1}\right)^{-1}\mathbf{C}^T \tilde{\mathbf{R}}_s^{-1}\left(\mathbf{y}_{1:\,t_s} - \mathbf{h}_{1:\,t_s}(\hat{\boldsymbol{\varphi}}_s^-)\right). \tag{12}$$

In this equation, $\hat{\boldsymbol{\varphi}}_s^+$ is the posterior mean estimate of $\boldsymbol{\varphi}_s$. The term $(\mathbf{C}^T \tilde{\mathbf{R}}_s^{-1}\mathbf{C} + (\hat{\mathbf{P}}_{\boldsymbol{\varphi},s}^-)^{-1})^{-1}\mathbf{C}^T \tilde{\mathbf{R}}_s^{-1}$ is referred to as the Kalman gain matrix [42] and is denoted by $\mathbf{K} \in \mathbb{R}^{(n_\theta + n_{w,t_s})\times(t_s \times n_y)}$ hereafter. The posterior covariance matrix can be obtained as follows (see [32] for derivation details):

$$\hat{\mathbf{P}}_{\boldsymbol{\varphi},s}^+ = (\mathbf{I} - \mathbf{KC})\hat{\mathbf{P}}_{\boldsymbol{\varphi},s}^-(\mathbf{I} - \mathbf{KC})^T + \mathbf{K}\tilde{\mathbf{R}}_s\mathbf{K}^T, \tag{13}$$

where $\mathbf{I} \in \mathbb{R}^{(n_\theta + n_{w,t_s})\times(n_\theta + n_{w,t_s})}$ is the identity matrix. The details for derivation of the Bayesian model updating and MAP formulations are similar to what has been used before in the literature [43–46].

In the rolling estimation window method, the posterior mean vector and the posterior covariance matrix of the extended estimation parameter vector at the $(s-1)^{\text{th}}$ estimation window are transferred to the s^{th} estimation window and used as prior information. The posterior mean vector and the posterior covariance matrix of the model parameters are transferred to the next estimation window directly and considered as prior estimates. However, the vehicular loads are divided into two groups. The first group includes the load of vehicles that enter the bridge between time step t_{s-1} and t_s. These are called new vehicles in the s^{th} estimation window and their associated load vector is denoted as $\mathbf{w}_{t_s}^{n}$. The initial vehicular load estimates can be different from the true values; and therefore, they will be estimated/updated through the joint estimation process. The second group includes the load of those vehicles that enter the bridge before t_{s-1}. These are called remaining vehicles, their associated load vector is presented as $\mathbf{w}_{t_s}^{r}$ and their posterior mean vector and covariance matrix are transferred from the previous estimation window and considered as priors. The mathematical detail of this process is further described.

The posterior mean vector at the $(s-1)^{\text{th}}$ estimation window and the prior mean vector at the s^{th} estimation window are partitioned as follows:

$$\widehat{\boldsymbol{\varphi}}_{s-1}^{+} = \left[\left(\widehat{\boldsymbol{\theta}}_{s-1}^{+}\right)^{T} \ \left(\widehat{\mathbf{w}}_{t_{s-1}}^{+,r}\right)^{T} \ \left(\widehat{\mathbf{w}}_{t_{s-1}}^{+,n}\right)^{T} \right]^{T}, \tag{14}$$

$$\widehat{\boldsymbol{\varphi}}_{s}^{-} = \left[\left(\widehat{\boldsymbol{\theta}}_{s}^{-}\right)^{T} \ \left(\widehat{\mathbf{w}}_{t_s}^{-,r}\right)^{T} \ \left(\widehat{\mathbf{w}}_{t_s}^{-,n}\right)^{T} \right]^{T}. \tag{15}$$

In equation (14), $\widehat{\boldsymbol{\theta}}_{s-1}^{+}$ is the posterior model parameter estimates at the $(s-1)^{th}$ estimation window. Vectors $\widehat{\mathbf{w}}_{t_{s-1}}^{+,r}$ and $\widehat{\mathbf{w}}_{t_{s-1}}^{+,n}$ are the posterior estimates for remaining and new vehicular loads at the $(s-1)^{th}$ estimation window, respectively. The term $\widehat{\boldsymbol{\theta}}_{s}^{-} = \widehat{\boldsymbol{\theta}}_{s-1}^{+}$ is the prior model parameter estimates at the s^{th} estimation window. The vector $\widehat{\mathbf{w}}_{t_s}^{-} = \left[(\widehat{\mathbf{w}}_{t_s}^{-,r})^{T} \ (\widehat{\mathbf{w}}_{t_s}^{-,n})^{T} \right]^{T}$ is the prior estimate for vehicular loads at the s^{th} estimation window, including the remaining and new vehicular loads. The term $\widehat{\mathbf{w}}_{t_s}^{-,r} = \left[(\widehat{\mathbf{w}}_{t_{s-1}}^{+,r})^{T} \ (\widehat{\mathbf{w}}_{t_{s-1}}^{+,n})^{T} \right]^{T}$ is the prior estimate for the remaining vehicular load vector at the s^{th} estimation window and includes the load of all the vehicles that enter the bridge before t_{s-1}. The term $\widehat{\mathbf{w}}_{t_s}^{-,n}$ include the initial load estimate of the vehicles that enter the bridge between time step t_{s-1} and t_s.

The partitioning of the posterior covariance matrix of the extended estimation parameter vector at the $(s-1)^{th}$ estimation window follows similar logic as

$$\widehat{\mathbf{P}}_{\boldsymbol{\varphi},s-1}^{+} = \begin{bmatrix} \left(\widehat{\mathbf{P}}_{\boldsymbol{\theta}\boldsymbol{\theta}}^{+}\right)_{s-1} & \left(\widehat{\mathbf{P}}_{\boldsymbol{\theta}\mathbf{w}^{r}}^{+}\right)_{s-1} & \left(\widehat{\mathbf{P}}_{\boldsymbol{\theta}\mathbf{w}^{n}}^{+}\right)_{s-1} \\ \left(\widehat{\mathbf{P}}_{\mathbf{w}^{r}\boldsymbol{\theta}}^{+}\right)_{s-1} & \left(\widehat{\mathbf{P}}_{\mathbf{w}^{r}\mathbf{w}^{r}}^{+}\right)_{s-1} & \left(\widehat{\mathbf{P}}_{\mathbf{w}^{r}\mathbf{w}^{n}}^{+}\right)_{s-1} \\ \left(\widehat{\mathbf{P}}_{\mathbf{w}^{n}\boldsymbol{\theta}}^{+}\right)_{s-1} & \left(\widehat{\mathbf{P}}_{\mathbf{w}^{n}\mathbf{w}^{r}}^{+}\right)_{s-1} & \left(\widehat{\mathbf{P}}_{\mathbf{w}^{n}\mathbf{w}^{n}}^{+}\right)_{s-1} \end{bmatrix}. \tag{16}$$

In equation (16), $(\widehat{\mathbf{P}}_{\mathbf{XY}}^{+})_{s-1}$ represents the posterior cross-covariance matrix of parameter vectors $\mathbf{X}$ and $\mathbf{Y}$ at the $(s-1)^{th}$ estimation window. The prior covariance matrix of the extended estimation parameter vector at the s^{th} estimation window is partitioned as follows:

$$\widehat{\mathbf{P}}_{\boldsymbol{\varphi},s}^{-} = \begin{bmatrix} \left(\widehat{\mathbf{P}}_{\boldsymbol{\theta}\boldsymbol{\theta}}^{-}\right)_{s} & \left(\widehat{\mathbf{P}}_{\boldsymbol{\theta}\mathbf{w}^{r}}^{-}\right)_{s} & \mathbf{0} \\ \left(\widehat{\mathbf{P}}_{\mathbf{w}^{r}\boldsymbol{\theta}}^{-}\right)_{s} & \left(\widehat{\mathbf{P}}_{\mathbf{w}^{r}\mathbf{w}^{r}}^{-}\right)_{s} & \mathbf{0} \\ \mathbf{0} & \mathbf{0} & \left(\widehat{\mathbf{P}}_{\mathbf{w}^{n}\mathbf{w}^{n}}^{-}\right)_{s} \end{bmatrix}. \tag{17}$$

It can be followed that $(\widehat{\mathbf{P}}_{\boldsymbol{\theta}\boldsymbol{\theta}}^{-})_{s} = (\widehat{\mathbf{P}}_{\boldsymbol{\theta}\boldsymbol{\theta}}^{+})_{s-1}$, $(\widehat{\mathbf{P}}_{\mathbf{w}^{r}\boldsymbol{\theta}}^{-})_{s} = (\widehat{\mathbf{P}}_{\boldsymbol{\theta}\mathbf{w}^{r}}^{-})_{s}^{T} = \begin{bmatrix} (\widehat{\mathbf{P}}_{\mathbf{w}^{r}\boldsymbol{\theta}}^{+})_{s-1} \\ (\widehat{\mathbf{P}}_{\mathbf{w}^{n}\boldsymbol{\theta}}^{+})_{s-1} \end{bmatrix}$ and $(\widehat{\mathbf{P}}_{\mathbf{w}^{r}\mathbf{w}^{r}}^{-})_{s} = \begin{bmatrix} (\widehat{\mathbf{P}}_{\mathbf{w}^{r}\mathbf{w}^{r}}^{+})_{s-1} & (\widehat{\mathbf{P}}_{\mathbf{w}^{r}\mathbf{w}^{n}}^{+})_{s-1} \\ (\widehat{\mathbf{P}}_{\mathbf{w}^{n}\mathbf{w}^{r}}^{+})_{s-1} & (\widehat{\mathbf{P}}_{\mathbf{w}^{n}\mathbf{w}^{n}}^{+})_{s-1} \end{bmatrix}$.

Also, the diagonal matrix $(\widehat{\mathbf{P}}_{\mathbf{w}^{n}\mathbf{w}^{n}}^{-})_{s}$ is the prior covariance matrix of $\mathbf{w}_{t_s}^{-,n}$ and should be initialized. As a summary, the process to setup the prior estimates at the s^{th} estimation window is shown schematically in Figure 3. As can be seen in this figure, the posterior mean vector and covariance matrix for model parameters at the $(s-1)^{\text{th}}$ estimation window are transferred as the prior mean vector and covariance matrix to the s^{th} estimation window. Moreover, the posterior mean vector and covariance matrix of the remaining and new vehicular loads at the $(s-1)^{\text{th}}$ estimation window are transferred to the s^{th} estimation window and augmented with those of the new vehicular load to yield the prior mean vector and covariance matrix of vehicular loads.

To increase the accuracy of the model updating technique and to find the correct posterior estimates of model parameters and vehicular loads, it is needed to iterate at each estimation window and update the prior estimates of the mean vector and covariance matrix of the extended estimation parameter vectors until they converge. To improve the convergence of the updating process, a diagonal matrix with small positive diagonal entries, represented by $\mathbf{Q}_s$, is added to the posterior covariance matrix to result in the prior covariance matrix for the next iteration [21].

$$\widehat{\mathbf{P}}_{\boldsymbol{\varphi},s,i+1}^{-} = \widehat{\mathbf{P}}_{\boldsymbol{\varphi},s,i}^{+} + \mathbf{Q}_s. \tag{18}$$

In equation (18), $\widehat{\mathbf{P}}_{\boldsymbol{\varphi},s,i}^{+}$ and $\widehat{\mathbf{P}}_{\boldsymbol{\varphi},s,i+1}^{-}$ denote the posterior covariance matrix at the i^{th} iteration and prior covariance matrix at the $(i+1)^{\text{th}}$ iteration at the s^{th} estimation window, respectively. In this study, the matrix $\mathbf{Q}_s$ is a diagonal matrix, in which the j^{th} diagonal entry is set to $q \times \boldsymbol{\varphi}_{s,j}$. The term $\boldsymbol{\varphi}_{s,j}$ is the j^{th} term of vector $\boldsymbol{\varphi}_s$, and q is a small constant scalar.

The initial estimates for model parameters, $\widehat{\boldsymbol{\theta}}_{0}^{+}$, are selected based on the prior information about model parameters obtained by engineering judgement from inspection reports. Moreover, assuming that the model parameters and vehicular loads are statistically independent, the initial covariance matrix of model parameters, $(\widehat{\mathbf{P}}_{\boldsymbol{\theta}\boldsymbol{\theta}}^{+})_{0}$, is initialized as a diagonal matrix, in which the j^{th} diagonal entry is the variance of the initial estimate of the j^{th} model parameter and is defined as $(p_{\boldsymbol{\theta}} \times \widehat{\boldsymbol{\theta}}_{0,j}^{+})^{2}$. In this definition, $\widehat{\boldsymbol{\theta}}_{0,j}^{+}$ is the j^{th} term of vector $\widehat{\boldsymbol{\theta}}_{0}^{+}$ and $p_{\boldsymbol{\theta}}$ is a scalar. Also, the matrix $(\widehat{\mathbf{P}}_{\mathbf{w}^{n}\mathbf{w}^{n}}^{-})_{s}$ is initialized as a diagonal matrix at the s^{th} estimation window, in which the j^{th} diagonal entry is the variance of the initial estimates of the new vehicular loads and is equal to $(p_{\mathbf{w}} \times \widehat{\mathbf{w}}_{t_s,j}^{-,n})^{2}$, where $\widehat{\mathbf{w}}_{t_s,j}^{-,n}$ is the j^{th} term of vector $\widehat{\mathbf{w}}_{t_s}^{-,n}$ and $p_{\mathbf{w}}$ is a scalar. The algorithmic details of the

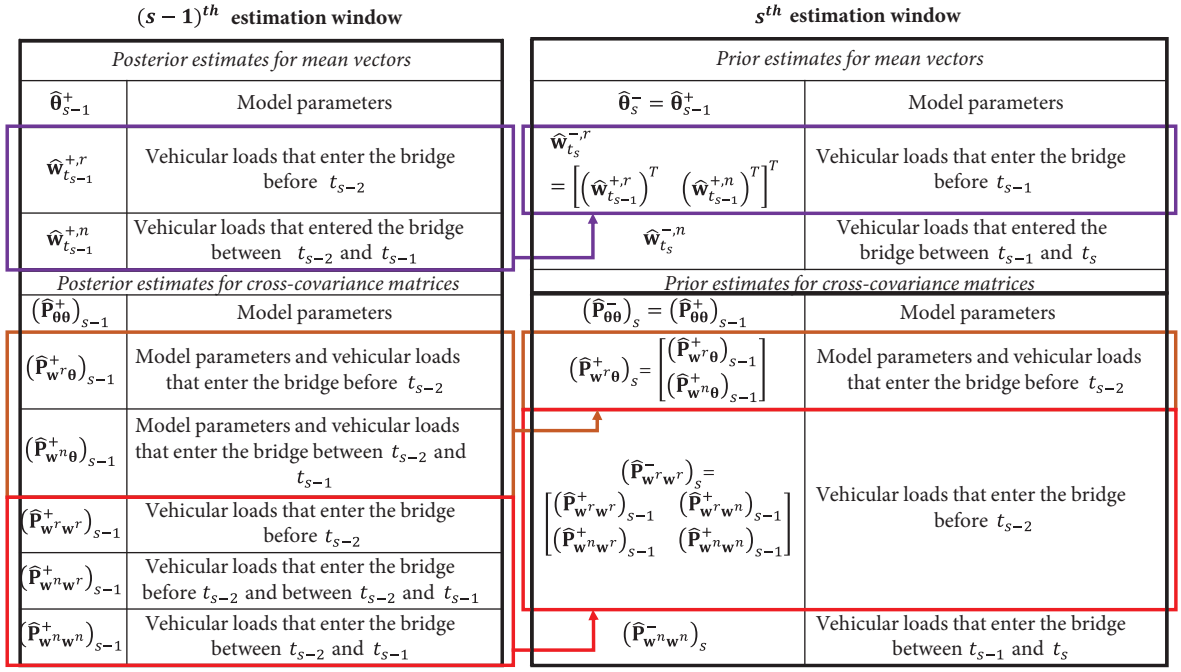

FIGURE 3: The process of transferring the posterior estimates at the $(s-1)^{\text{th}}$ estimation window to the prior estimates at the s^{th} estimation window.

proposed Bayesian FE model updating technique is summarized in Table 1.

4. Damage Mechanisms in Prestressed Concrete Box-Girder Bridges

To identify the severity and extent of damage from the updated model parameters, it is necessary to understand how different mechanisms of damage may affect the mechanical properties of the bridge and how they can be reflected in the FE model. Therefore, the common damage mechanisms in prestressed concrete box-girder bridges and their modeling strategies are discussed in this section.

4.1. Concrete Deterioration. Concrete deterioration may happen over time as a result of chemical (e.g., deicing salts) and/or physical (e.g., freeze-and-thaw) attacks to the concrete matrix, and lead to degradation of mechanical properties (e.g., stiffness and strength) of reinforced and prestressed concrete members [47, 48]. Therefore, localizing and quantifying concrete deterioration is essential to decide the maintenance or replacement of bridge members. Concrete deterioration can be classified as delamination and degradation (see Figure 4). Concrete delamination is the horizontal debonding between rebar and concrete as a consequence of expansion in corroded rebars [50, 51]. It results in the reduction of the effective concrete thickness, and if happens in bridge decks, can lead to the loss of flexural stiffness and strength of the bridge [52]. Hence, in the FE model of the bridge, concrete delamination in top slab (deck) is simulated by reducing the concrete thickness, th_c (discussed in detail in §5.1). As listed in Table 2, four delamination damage states are defined following the Minnesota Department of Transportation inspection manual. The damage states criteria are determined based on the ratio of the effective to the nominal (design) thickness of the deck concrete [53].

Concrete degradation may happen as a result of several factors, including reinforcement corrosion and alkali-silica reaction, which develop cracks in the concrete matrix and reduce its compressive strength and stiffness [49, 51, 54]. So, in the FE model of the bridge, concrete degradation in bridge deck and girders is simulated through the reduction of concrete compressive strength, denoted as f_c' in Figure 5. In this figure the terms f_t', f_{cu}', E_c, ε_c, and ε_{cu} are the concrete tensile strength, crushing strength, initial stiffness, strain at compressive strength, and strain at crushing strength, respectively. Reduction in the concrete compressive strength results in the reduction of stiffness and tensile and crushing strength of the concrete material model. A study on the concrete degradation reported an ultimate reduction of 27.6% in f_c' in natural environment over a period of six years [55]. Moreover, studies on the durability of concrete subjected to harsh acidic environments have reported up to 28% reductions in f_c' [56]. According to the same studies, it is concluded that a *severe* concrete degradation may result in 25% or more reduction in f_c'. Moreover, in [57], a model has been developed for reduction of f_c' due to concrete degradation. The study suggested that the reduction rate of f_c' in degraded concrete increases sharply after 15% reduction. So, 15% to 25% reduction in f_c' is assumed to represent a *mild* concrete degradation in this study. Moreover, up to 5% reduction in f_c' is expected to have minor adverse effects on

Table 1: The proposed Bayesian FE model updating algorithm.

(1) Initialization:
(1.1). Set the initial values for $\widehat{\boldsymbol{\theta}}_0^+$ and $(\widehat{\mathbf{P}}_{\boldsymbol{\theta}\boldsymbol{\theta}}^+)_0$
(1.2). Set $t_0 = 1$
(1.3). Set $\widehat{\boldsymbol{\varphi}}_0^+ = \widehat{\boldsymbol{\theta}}_0^+, \widehat{\mathbf{P}}_{\boldsymbol{\varphi},0}^+ = (\widehat{\mathbf{P}}_{\boldsymbol{\theta}\boldsymbol{\theta}}^+)_0, \widehat{\mathbf{w}}_0^{+,r} = \mathbf{0}, \widehat{\mathbf{w}}_0^{+,n} = \mathbf{0}$, $(\widehat{\mathbf{P}}_{\mathbf{w}^r\boldsymbol{\theta}}^+)_0 = \mathbf{0}$, $(\widehat{\mathbf{P}}_{\mathbf{w}^n\boldsymbol{\theta}}^+)_0 = \mathbf{0}$, $(\widehat{\mathbf{P}}_{\mathbf{w}^n\mathbf{w}^r}^+)_0 = \mathbf{0}$, $(\widehat{\mathbf{P}}_{\mathbf{w}^r\mathbf{w}^r}^+)_0 = \mathbf{0}$, and $(\widehat{\mathbf{P}}_{\mathbf{w}^n\mathbf{w}^n}^+)_0 = \mathbf{0}$
(2) For the s^{th} estimation window $(s = 1, 2, \ldots, n_s)$:
(2.1). Set t_s.
(2.2). Retrieve the posterior mean vector and covariance matrix of the extended estimation parameter vector from the $(s-1)^{th}$ estimation window $(\widehat{\boldsymbol{\varphi}}_{s-1}^+, \widehat{\mathbf{P}}_{\boldsymbol{\varphi},s-1}^+)$
(2.3). Detect the vehicles that enter the bridge between time step t_{s-1} and t_s and initialize the associated prior mean vector and covariance matrix of vehicular loads $(\widehat{\mathbf{w}}_{t_s}^{-,n}, (\widehat{\mathbf{P}}_{\mathbf{w}^n\mathbf{w}^n}^-)_s)$.
(2.4). Transfer posterior estimates from the $(s-1)^{\text{th}}$ estimation window and find the prior mean vector (equation (15)) and prior covariance matrix (equation (17)) of the extended estimation parameter vector
(2.5). Find $\widetilde{\mathbf{R}}_s$ (equation (9)) and $\mathbf{Q}_s$.
(2.6). Initialize for iteration: set $\widehat{\boldsymbol{\varphi}}_{s,0}^+ = \widehat{\boldsymbol{\varphi}}_s^-$ and $\widehat{\mathbf{P}}_{\boldsymbol{\varphi},s,0}^+ = \widehat{\mathbf{P}}_{\boldsymbol{\varphi},s}^-$
(2.7). Iterate $(i = 1, 2, \ldots)$:
(2.7.1). Set $\widehat{\boldsymbol{\varphi}}_{s,i}^- = \widehat{\boldsymbol{\varphi}}_{s,i-1}^+$ and $\widehat{\mathbf{P}}_{\boldsymbol{\varphi},s,i}^- = \widehat{\mathbf{P}}_{\boldsymbol{\varphi},s,i-1}^+ + \mathbf{Q}_s$
(2.7.2). Run the FE model using $\widehat{\boldsymbol{\varphi}}_{s,i}^-$ to derive the FE response and response sensitivities, i.e., $\widehat{\mathbf{y}}_{1:t_s} = \mathbf{h}_{1:t_s}(\widehat{\boldsymbol{\varphi}}_{s,i}^-)$ and $\mathbf{C} = \partial \mathbf{h}_{1:t_s}(\boldsymbol{\varphi}_s)/\partial \boldsymbol{\varphi}_s|_{\boldsymbol{\varphi}_s = \widehat{\boldsymbol{\varphi}}_{s,i}^-}$
(2.7.3). Compute the Kalman gain matrix: $\mathbf{K} = (\mathbf{C}^T \widetilde{\mathbf{R}}_s^{-1} \mathbf{C} + (\widehat{\mathbf{P}}_{\boldsymbol{\varphi},s,i}^-)^{-1})^{-1} \mathbf{C}^T \widetilde{\mathbf{R}}_s^{-1}$
(2.7.4). Derive the posterior mean vector and posterior covariance matrix of the extended estimation parameter vector, i.e., $\widehat{\boldsymbol{\varphi}}_{s,i}^+ = \widehat{\boldsymbol{\varphi}}_{s,i}^- + \mathbf{K}(\mathbf{y}_{1:t_s} - \widehat{\mathbf{y}}_{1:t_s})$, $\widehat{\mathbf{P}}_{\boldsymbol{\varphi},s,i}^+ = (\mathbf{I} - \mathbf{KC})\widehat{\mathbf{P}}_{\boldsymbol{\varphi},s,i}^- (\mathbf{I} - \mathbf{KC})^T + \mathbf{K}\widetilde{\mathbf{R}}_s \mathbf{K}^T$
(2.7.5). Check for convergence. If $|\widehat{\boldsymbol{\varphi}}_{s,i}^+ - \widehat{\boldsymbol{\varphi}}_{s,i-1}^+| < tol1 \times |\widehat{\boldsymbol{\varphi}}_{s,i-1}^+|$ or $i > tol2$, where $tol1$ is the tolerance limit for relative change in the extended estimation parameter vector and $tol2$ is the maximum number of iterations, then move to the next estimation window: set $\widehat{\boldsymbol{\varphi}}_s^+ = \widehat{\boldsymbol{\varphi}}_{s,i}^+$ and $\widehat{\mathbf{P}}_{\boldsymbol{\varphi},s}^+ = \widehat{\mathbf{P}}_{\boldsymbol{\varphi},s,i}^+$, $s = s + 1$, and go to step 2. Otherwise, iterate again in the current estimation window: set $i = i + 1$ and go to step 2.7

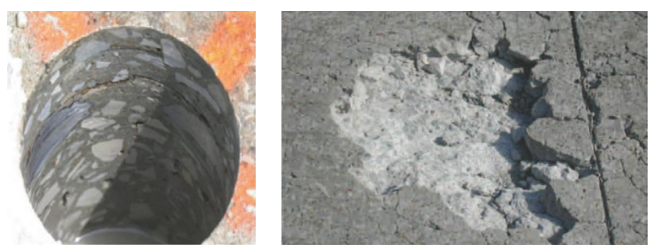

(a) (b)

Figure 4: Concrete deterioration: (a) bridge deck delamination in a drilled hole and (b) bridge deck degradation due to alkali-silica reaction [49].

Table 2: Proposed damage state and color codes for different damage mechanisms based on the ratio of the damaged to nominal (design) parameter value.

Color code	Damage state	th_c	f_c'	th_s	PF
	No damage	1.00	>0.95	>0.9	>0.95
	Minor damage	<1.00	≤0.95	<0.90	≤0.95
	Mild damage	<0.85	≤0.85	<0.80	≤0.84
	Severe damage	≤0.67	≤0.75	<0.70	≤0.70

th_c: top slab concrete thickness, f_c': concrete compressive strength, th_s: top slab smeared steel layer thickness, and PF: prestressing force.

the bridge response. So, 5% to 15% reduction in f_c' is considered as *minor* concrete degradation and less than 5% reduction is categorized as *no damage* state. A summary of the proposed degradation damage states and color codes are provided in the fourth column of Table 2.

4.2. Reinforcement Corrosion. Another primary consequence of reinforcement corrosion in bridge decks is the loss of cross-sectional area of steel and steel-concrete bond, which may affect the flexural strength in negative moment regions (e.g., on top of piers, where the top slab endures tensile flexural stress). The slab reinforcement in the FE model are simulated with an equivalent smeared layer, and its corrosion is simulated by reducing the thickness of the smeared steel layer at top slab, th_s (discussed in detail in §5.1). The corrosion damage state can be quantified based on Zhu [51], in which an experimental test was performed on reinforced beams subjected to chloride environments for 14,

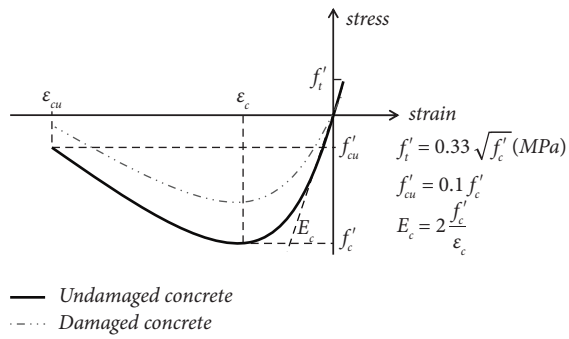

Figure 5: Stress-strain model of concrete material and how reduction in f_c' simulates concrete degradation.

23, 26, and 28 years. The results showed more than 30% reduction in steel cross-sectional area in the most severe cases. So, 30% loss in th_s is considered as the upper bound for *severe* corrosion state in this study. Other corrosion damage states are defined as a linear function of loss in th_s, i.e., up to 10% loss indicates *no damage* state, up to 20% loss represents *minor* steel corrosion, and up to 30% shows *mild* steel corrosion damage state.

4.3. Loss of Prestressing Force. The high-strength steel tendons, which are used in pretensioned or posttensioned systems, can experience corrosion, which can also lead to microcracking and deterioration of the bond between concrete and tendons as a result of the loss of prestressing force [58]. This damage mechanism is simulated through a reduction in the prestressing force (*PF*). Study of accelerated corroded prestressed beams exhibited up to 50% reduction in prestressing force [58]. Based on this study, over 30% reduction in *PF* is considered as *severe* loss of prestressing force herein. Also, a *mild* damage state is defined as 16 to 30% loss in *PF*, and 5 to 16% loss is defined as *minor* damage state. Moreover, loss of prestressing force less than 5% is considered as a *no damage* state. The corresponding limits and color codes are provided in the last column of Table 2.

5. Verification Study Using Numerically Simulated Data

The proposed Bayesian FE model updating technique for operational monitoring and damage identification is verified through examination of 10 different numerically simulated damage scenarios for a prestressed concrete box-girder bridge subjected to traffic load. The verification study process is as follows: First, a mechanics-based nonlinear FE model of the bridge is developed in OpenSees [59]. The FE model is parametrized to simulate various damage mechanisms as discussed in the previous section. Then, an identifiability analysis [60] is performed to find the likely identifiable model parameters and the most informative measurement locations. After that, the acceleration responses of the bridge are simulated to a random traffic load scenario and polluted with artificial measurement noises to result in the measured responses. In the next step, the measured responses and the location of vehicles on the bridge are fed into the Bayesian FE model updating technique, which is implemented in MATLAB [61] interfacing with OpenSees [59] to jointly estimate the vehicular loads and model parameters. The final estimates of the model parameters are used to infer damage states along the bridge, which is then compared with the simulated damage states to evaluate the efficacy of the proposed technique. Details of the developed FE model are discussed in Section 5.1. The process to simulate the traffic load is presented in Section 5.2. Following that, the identifiability assessment and the 10 simulated damage scenarios are described. Finally, the damage identification outcomes are presented and discussed in Section 5.5.

5.1. Finite Element Model of the San Roque Canyon Bridge. The bridge model used in this study is based on the San Roque Canyon (SRC) highway overpass bridge, which is located in Santa Barbara County, CA, and was built in 1984. SRC is a prestressed reinforced concrete box-girder bridge and a representative of a large inventory of aging box-girder bridges in the west coast U.S., which are prone to concrete deterioration, reinforcement corrosion, loss of prestressing force, and subsequent structural damage.

The SRC is a three-span straight and continuous bridge with a 14 m-wide deck supporting two lanes of traffic (one lane in each direction). The midspan is 61 m-long and the two adjacent spans are 44 m-long. The superstructure consists of five box girders with 2 m depth and 300 mm web thickness. The top and bottom slabs are 200 mm and 160 mm thick with #4@230 mm and #5@470 mm longitudinal reinforcement, respectively.

Based on the as-built structural drawings, a detailed FE model of the bridge is created in OpenSees. Since the present study is focused on the dynamics of the bridge under traffic load, the soil-foundation and soil-abutments are not included in the model for simplification. Piers are fixed-base and abutments are modeled with roller supports. Piers are modeled with elastic beam-column elements with modulus of elasticity of 27.8 GPa and a Caltrans octagon cross-section with 2 m depth and 3.2 m width. Girders are modeled using fiber-section displacement-based beam-column elements, with an approximate length of 4 m, and five integration points. Moreover, the linear-elastic shear and torsional stiffness of the girders are calculated and aggregated on the fiber sections. The tendons in the girders have a nominal

cross-sectional area of 5335 mm^2 each. To accurately model the tendon profile, the depth of the tendon at the integration points of each element is determined based on the as-built drawings. Top and bottom slabs are modeled using layered quadrilateral shell elements (*ShellDKGQ*) with an approximate mesh size of 4 m × 2.5 m, and the slab reinforcements are modeled using smeared steel layers [62]. Top and bottom shell elements are connected to the beam-column element nodes using rigid links. The concrete is modeled using *Concrete02* material with nominal compressive strength of 34.5 MPa, strain at maximum strength of 0.2%, strain at crushing strength of 2% –other parameters are defined based on Figure 5. The reinforcing steel is modeled using *steel*02 material with modulus of elasticity of 200 GPa. Moreover, the initial strain of 0.66% due to the prestressing force in tendons is assigned to the corresponding *steel*02 material using *InitStrainMaterial*. In summary, the FE model consists of 150 beam-column elements, 300 shell elements, 597 joints, and 3510 degrees of freedom. A view of the final model with prestressing forces applied and a schematic representation of the superstructure are illustrated in Figure 6. The figure clearly presents the upward camber due to the prestressing forces. Rayleigh damping is modeled considering 5% damping ratio for the first and the fifth vertical modes. To simulate the nonlinear response of the bridge to the traffic load, the nonlinear time history analysis is performed using the Newmark average acceleration method with a constant time step size of 0.01 seconds. The Newton–Raphson method is used to iteratively solve the nonlinear equilibrium equations.

5.2. Traffic Load Simulation. To simulate the traffic load, an algorithm is developed to simulate random realistic traffic scenarios and calculate the resulting time history of nodal loads that will be applied to the bridge model. The developed algorithm generates a sequence of vehicles with random loads. The loads have a uniform distribution function ranging from 8 kN for motorbikes to 50 kN for light/medium trucks with lengths of 2 m to 5 m, respectively. Vehicles have a random speed with a uniform distribution function between 25 m/s to 35 m/s. However, to avoid overtaking on the bridge, it is assumed that a vehicle cannot travel faster than the one ahead. With this condition, each vehicle's speed is considered as the minimum value of the randomly generated speed and speed of the vehicle ahead. A random safety time with a uniform distribution between 3.0 and 3.1 seconds is maintained between the vehicles. This could be shown as follows:

$$ET_i = \mathrm{fix}\left[\frac{1}{dt} \times \left(ET_{i-1} + \frac{l_{i-1}/2}{v_{i-1}} + ST_i\right)\right] \times dt, \tag{19}$$

where ET_i is the entrance time for the i^{th} vehicle. Function $\mathrm{fix}[X]$ rounds the value of X to the nearest integer toward zero. Parameter dt is the sampling time step (0.01 second here). Parameters l_{i-1} and v_{i-1} are the length and speed of the $(i-1)^{\text{th}}$ vehicle and parameter ST_i is the safety time between the $(i-1)^{\text{th}}$ and i^{th} vehicles. Center of gravity of vehicles is coincided with the mesh lines at the middle of each traffic lane. To calculate the time history of the traffic load, the total time duration of traffic is divided into multiple time steps. At each time step, the load of each vehicle (applied at its center of gravity) is distributed to the nodes of adjacent shell elements. The share of vehicular load transferred to each node is linearly proportional to the distance between the node and the vehicle. Further details are presented in Figure 7. Finally, the resultant nodal loads are added up at each node to yield the nodal load time history for the simulated traffic scenario. This vehicular load distribution method is later used in identifiability analysis and forward simulations, as well as model updating process.

5.3. Identifiability Assessment. Identifiability assessment is a critical step in any model updating process to find the likely identifiable model parameters and decide about the most informative sensor arrangement. An information-theoretic approach for identifiability assessment based on [60] is used in this study. In this approach, the amount of information that each FE model parameter receives from the measurement data and the mutual correlation between parameter pairs are evaluated. The FE model parameters that receive little or no information or are strongly correlated with other parameters are likely to be poorly identifiable. Therefore, they will be excluded from the parameters that are intended to be identified through the model updating process. Moreover, the amount of information that different measurement channels carry about the model parameters are used to decide about the location of measurement channels along the bridge.

In the first step, the most general parametrization scheme for the SRC bridge model with 25 model parameters is considered for identifiability assessment. These parameters include prestressing force (PF), compressive strength of girders and top slab ($f_c^{'g}$ and $f_c^{'d}$), top slab concrete thickness (th_c), and top slab smeared steel layer thickness (th_s) at 5 different regions along the bridge. According to Figure 8, regions 1, 3, and 5 are the positive moment regions, where the top slab is expected to be in compression under operational loads. Regions 2 and 4 are the negative moment regions, where the top slab is susceptible to tensile cracking and the subsequent deterioration and rebar corrosion. In this study, the corresponding length of regions 1 to 5 is set to 39.50, 10.62, 48.76, 10.62, and 39.50 m, respectively. The nominal values of the model parameters are presented in Table 3. Moreover, 15 possible locations for acceleration measurement channels are considered on the bridge as shown in Figure 8.

To run the identifiability assessment, a random traffic scenario is simulated on the bridge FE model and the sensitivity of the measured responses with respect to each model parameter at its nominal value is computed. The resulting sensitivity matrix is used to calculate the relative entropy gain of each model parameter and the mutual entropy gains between parameter pairs based on [60]. These results are presented in Figures 9(a) and 9(b), respectively. For a better understanding of the dependencies between parameter pairs in Figure 9(b), the values on each row are normalized to their corresponding diagonal value and then the diagonals are nullified (actual values are replaced by zero). This normalization method results in an

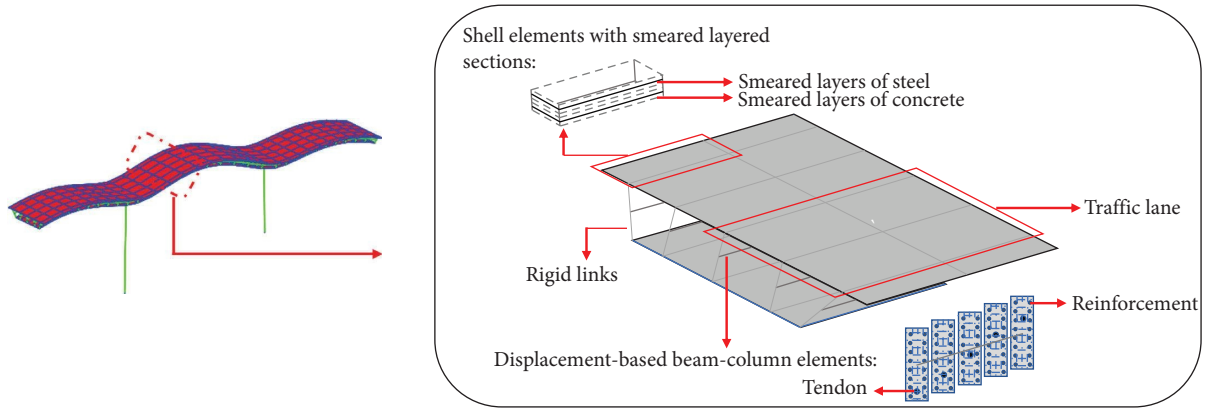

Figure 6: FE model of the SRC bridge: (a) bridge camber after applying the prestressing forces and (b) schematic presentation of the superstructure modeling details.

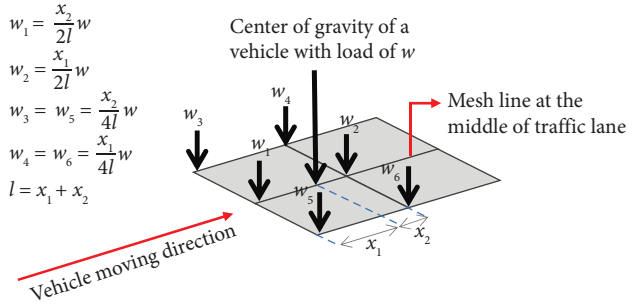

Figure 7: Distribution of the vehicular load to the shell elements' nodes.

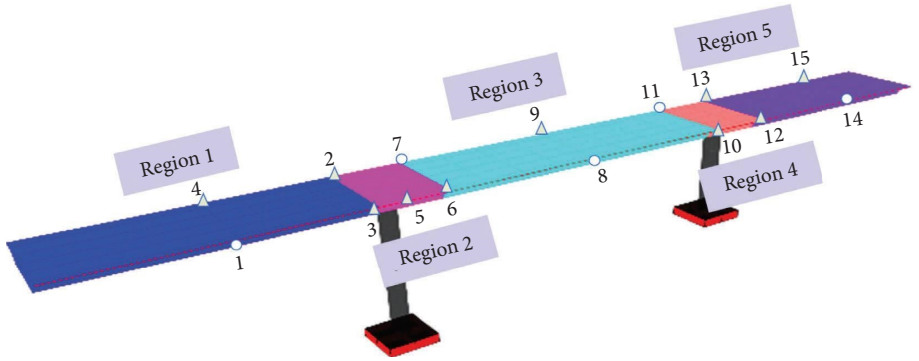

Figure 8: Different regions defined based on the expected moment diagram of the bridge. Markers represent the location of measurement channels used in the identifiability assessment. Among the markers, the five locations shown with circular markers are selected for model updating.

Table 3: List of model parameters used for identifiability assessment and their nominal values.

Parameter ID	Description	Nominal value
1–5	Prestressing force in regions 1 to 5, respectively (PF)	6.90 MN
6–10	Effective compressive strength of girders in regions 1 to 5, respectively ($f_c^{'g}$)	34.5 MPa
11–15	Effective compressive strength of top slab in regions 1 to 5, respectively ($f_c^{'d}$)	34.5 MPa
16–20	Top slab concrete thickness in regions 1 to 5, respectively (th_c)	199.5 mm
21–25	Top slab smeared steel layer thickness in regions 1 to 5, respectively (th_s)	0.5 mm

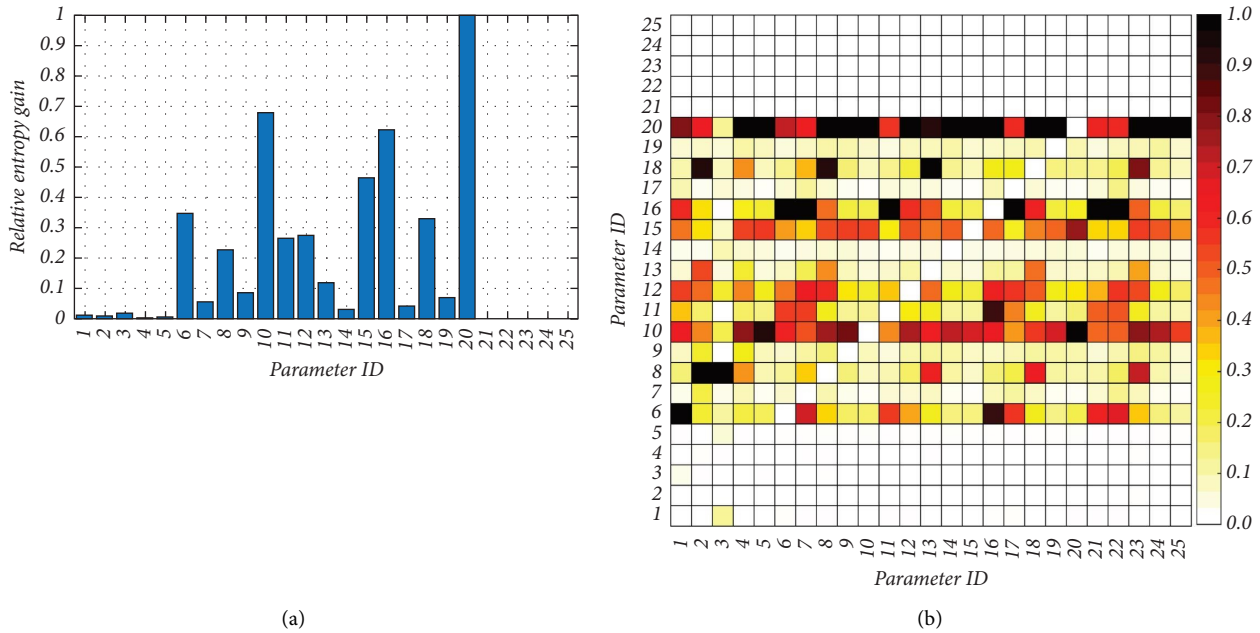

(a) (b)

FIGURE 9: Identifiability assessment results: (a) relative entropy gains and (b) relative mutual entropy gain between parameter pairs. In part (b), first each row is normalized to the corresponding diagonal value and then the diagonals are nullified to help the presentation.

asymmetrical representation for the relative mutual entropy gains.

As can be observed in Figure 9(a), parameters 16–20 that represent the top slab concrete thickness (th_c) in regions 1 to 5, respectively, have a considerable relative entropy gain. However, as can be seen in Figure 9(b), these parameters are correlated with other parameters, especially 6–10 and 11–15, representing compressive strength of girders ($f_c'^g$) and top slab ($f_c'^d$) in regions 1 to 5, respectively. This is due to the simultaneous effect of concrete compressive strength and its thickness on the stiffness and, thus, dynamic response of the bridge. Therefore, distinguishing between top slab concrete thickness and its compressive strength is not possible. This means that either th_c or $f_c'^d$ should be fixed. The normalized relative mutual entropy gains between the parameters th_c and $f_c'^d$ in Figure 9(b) suggests that the parameters th_c have greater dependency on the parameters $f_c'^d$. Consequently, in the model updating process, the top slab concrete thickness (th_c) is fixed, and its compressive strength ($f_c'^d$) is estimated.

Parameters 6–10 ($f_c'^g$) with considerable relative entropy gain and low dependency on other parameters are selected as model parameters to estimate concrete degradation in girders. Moreover, parameters 21–25, which represent the thickness of smeared steel layer at top slab (th_s) in regions 1 to 5, respectively, have negligible relative entropy gains. This is also due to their minor effect on the dynamic response of the bridge under the traffic load. So, the five th_s parameters are fixed through the model updating process. However, as stated in Section 4.1, steel corrosion can result in concrete degradation. Hence, the top slab reinforcement corrosion could be implicitly screened through the reduction in compressive strength ($f_c'^d$).

Parameters 1–5 that represent prestressing force (PF) in regions 1 to 5, respectively, have relatively low entropy gains. However, as can be noticed in Figure 9(b), these parameters have little dependency on other parameters. So, they are included in the model parameters; but, uncertainty in the estimated values is expected to be large due to their low relative entropy gain.

As a summary, all the parameters th_s,th_c,PF,$f_c'^g$, and $f_c'^d$ are used in the forward simulations to simulate damage in the bridge. Concrete degradation in girders and top slab is simulated and estimated through $f_c'^g$ and $f_c'^d$, respectively. However, as discussed, the parameters th_c and th_s cannot be estimated in the model updating process and are excluded from the model parameters to be estimated. On the other hand, concrete delamination and steel corrosion have simultaneous effects on parameters th_c and $f_c'^d$, and th_s and $f_c'^d$, respectively (see §4). So, while concrete delamination and steel corrosion are simulated through parameters th_c and th_s, respectively, these damage mechanisms are implicitly estimated through the parameters $f_c'^d$. Moreover, it should be noted that in the Bayesian FE model updating technique, the parameters th_c and th_s are fixed at their nominal (design) values. Finally, tendon corrosion and bond deterioration are simulated and estimated through PF. Hereafter, the term "model parameters" is exclusively used to refer to the parameters that are estimated in the FE model updating process (i.e., PF,$f_c'^g$, and $f_c'^d$ in five regions). This results in 25 parameters for damage simulation and 15 model parameters for the FE model updating.

At the next step, the total entropy gain of the selected 15 model parameters is calculated for each candidate measurement channel and presented in Figure 10. As can be observed, channels 1 and 4 provide information for parameters $f_c'^g$ and $f_c'^d$. Since these channels have symmetric location with respect to the centroid line of the bridge in its longitudinal direction (see Figure 8), only one of them, channel 1 herein, is selected. Measurement channels 2, 3, and 5 provide small entropy gain for the model parameters

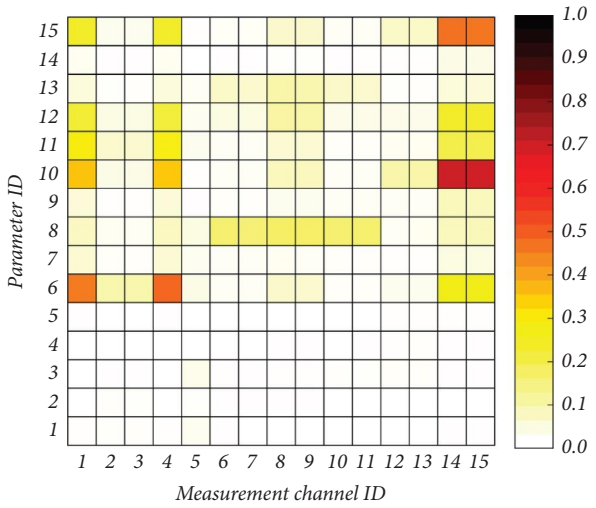

FIGURE 10: Relative entropy gains of 15 model parameters from 15 suggested measurement channels.

and are not deemed useful. Measurement channels 6 and 7 provide a higher entropy gain than measurement channel 1 for parameters 8 and 13, and so they are selected. However, since they are located symmetrically, only one of them is selected, (channel 7 herein). Measurement channels 8 and 9 provide the largest entropy gain for model parameter 13, and because of their symmetric location, only measurement channel 8 is selected. Between measurement channels 10 and 11, which are informative about model parameter 8, channel 11 is selected. None of the measurement channels 12 and 13 are selected due to their relatively low information content. Finally, between measurement channels 14 and 15, which both contain valuable information about parameters 6–10 and 11–15, the measurement channel 14 is selected. The final locations of selected measurement channels are shown in Figure 8 with circular marks.

5.4. Damage Scenarios. In this study, 10 unique damage scenarios are defined to verify the damage identification capability of the proposed approach (see Table 4). The parameters that are used in the simulation of damage but are not estimated through the model updating process are listed in this table using bold fonts. The presented scenarios represent a wide range of damage conditions starting from localized minor damage (e.g., D01) to extensive distributed damage (e.g., D06). These scenarios are included to examine the performance of the proposed approach in identifying various simple to complex damage conditions. Each damage scenario is modeled by altering the parameter values from their nominal to the corresponding true values, which is used to simulate damage. The simulated loss for each parameter in Table 4 is defined as follows:

$$\text{Simulated Loss (S.L.) (\%)} = \left(1 - \frac{\text{True value}}{\text{Nominal value}}\right) \times 100. \tag{20}$$

5.5. Bayesian FE Model Updating and Damage Identification Results. The Bayesian FE model updating technique presented in Table 1 is implemented using 20 seconds of acceleration measurement data. The FE simulated acceleration responses are polluted with artificial zero-mean Gaussian noises with root mean square (RMS) noise-to-signal ratio of 4%. Considering a sampling rate of 100 Hz for measurements, the input time history is divided into 20 rolling estimation windows (i.e., $n_s = 20$-see Table 1) with constant rolling rate of 100 time steps (i.e., $t_1 = 100$ and $t_s - t_{s-1} = 100, \forall s \geq 2$). The relative initial error (RIE) for each model/vehicular load parameter is defined as follows:

$$\text{Relative Initial Error (RIE) (\%)} = \left(\frac{\text{Initial value}}{\text{True value}} - 1\right) \times 100. \tag{21}$$

The RIE represents the difference between the initial estimates of model and vehicular load parameters ($\widehat{\boldsymbol{\theta}}_0^+$ or $\widehat{\mathbf{w}}_{t_s}^{-,n}$) and their corresponding true values. To set the initial covariance matrix of model parameters $(\widehat{\mathbf{P}}_{\boldsymbol{\theta}\boldsymbol{\theta}}^+)_0$, the term $p_{\boldsymbol{\theta}}$ is set to 0.1. Moreover, to form the prior covariance matrix of new vehicles at each estimation window (i.e., $(\widehat{\mathbf{P}}_{\mathbf{w}^n\mathbf{w}^n}^-)_s, \forall s$), the term $p_{\mathbf{w}}$ is set to 0.1. The variance of the measurement noise at all channels (i.e., the diagonal entries of the simulation error covariance matrix $\mathbf{R}$) are assumed to be time-invariant and equal to $(0.03\%g)^2$. To form matrix $\mathbf{Q}_s$ at each estimation window, the term q is set to 10^{-9}. The tolerance limits tol1 and tol2 do not have a significant effect on the model updating results. However, it is noteworthy that an increase in tol1 and a decrease in tol2 would reduce both the computational cost and accuracy of the results. The authors' preliminary studies have shown that $tol1 = 0.0015$ and $tol2 = 16$ are reasonable values for this specific problem. Further increasing the number of iterations or decreasing the tolerance does not significantly change the results. Also, the constrained correction approach based on [32] is implemented in the Bayesian FE model updating technique. This is to avoid the estimation of unphysical parameter values, and to improve the convergence and robustness of the algorithm. The lower bound for model parameter and vehicular load estimates are 0.1 of the initial estimates and the upper bounds are 10 times of the initial estimates. The model updating process is carried out in 5 hours using parallel processing scheme with 30 CPU threads. In this section, the model updating results for the simulated damage scenario D03 is presented in details first, and then the results for all damage scenarios are provided in a tabulated format and further discussed.

Damage scenario D03 represents severe degradation and delamination in top slab and girders in region 2 and includes mild corrosion in top slab reinforcements and tendons in girders in this region. The true damage state and color code for each region is defined based on the most severe damage state in that region and is shown in Figure 11 for damage scenario D03. In this figure, for each parameter, the simulated loss is shown in the second column of the tables.

Table 4: Details of the damage scenarios.

Damage scenario I.D.	Parameter I.D.	S.L. (Eq. (20)) Region 1	2	3	4	5	Description
D01	$f_c'^d$	0	10	0	0	0	Minor degradation in top slab and girders, localized in region 2
	$f_c'^g$	0	10	0	0	0	
	PF	0	0	0	0	0	
	$\mathbf{th}_s$	0	0	0	0	0	
	$\mathbf{th}_c$	0	0	0	0	0	
D02	$f_c'^d$	0	20	0	0	0	Mild degradation in girders and top slab and mild delamination in top slab resulted from severe top slab reinforcement corrosion, localized in region 2
	$f_c'^g$	0	15	0	0	0	
	PF	0	0	0	0	0	
	$\mathbf{th}_s$	0	40	0	0	0	
	$\mathbf{th}_c$	0	30	0	0	0	
D03	$f_c'^d$	0	30	0	0	0	Severe degradation in girders and top slab and severe delamination in top slab resulted from mild corrosion in top slab reinforcement, and mild loss in prestressing force due to tendon corrosion, localized in region 2
	$f_c'^g$	0	30	0	0	0	
	PF	0	20	0	0	0	
	$\mathbf{th}_s$	0	25	0	0	0	
	$\mathbf{th}_c$	0	40	0	0	0	
D04	$f_c'^d$	10	5	10	10	10	Minor degradation in top slab and girders, distributed along the bridge
	$f_c'^g$	10	5	5	5	10	
	PF	0	0	0	0	0	
	$\mathbf{th}_s$	0	0	0	0	0	
	$\mathbf{th}_c$	0	0	0	0	0	
D05	$f_c'^d$	20	20	15	20	20	Mild degradation in top slab and girders and minor prestressing force loss due to tendon corrosion, distributed along the bridge
	$f_c'^g$	15	20	15	15	20	
	PF	10	10	5	15	10	
	$\mathbf{th}_s$	0	0	0	0	0	
	$\mathbf{th}_c$	0	0	0	0	0	
D06	$f_c'^d$	5	10	5	10	5	Minor degradation in girders and top slab and minor delamination in top slab resulted from mild top slab reinforcement and tendon corrosion, distributed along the bridge
	$f_c'^g$	5	10	5	10	5	
	PF	20	25	20	25	20	
	$\mathbf{th}_s$	25	30	25	30	25	
	$\mathbf{th}_c$	5	10	5	19	5	
D07	$f_c'^d$	0	0	0	0	0	Minor delamination resulted from minor top slab reinforcement corrosion, localized in region 2
	$f_c'^g$	0	0	0	0	0	
	PF	0	0	0	0	0	
	$\mathbf{th}_s$	0	20	0	0	0	
	$\mathbf{th}_c$	0	10	0	0	0	
D08	$f_c'^d$	0	25	0	0	0	Severe delamination and severe degradation in top slab resulted from severe top slab reinforcement corrosion, localized in region 2
	$f_c'^g$	0	0	0	0	0	
	PF	0	0	0	0	0	
	$\mathbf{th}_s$	0	50	0	0	0	
	$\mathbf{th}_c$	0	50	0	0	0	
D09	$f_c'^d$	0	0	0	0	0	Bond deterioration between concrete and tendon resulted in mild and minor prestressing force loss, distributed along the bridge
	$f_c'^g$	0	0	0	0	0	
	PF	25	15	15	15	25	
	$\mathbf{th}_s$	0	0	0	0	0	
	$\mathbf{th}_c$	0	0	0	0	0	
D10	$f_c'^d$	0	0	0	0	0	Mild tendon corrosion, distributed along the bridge
	$f_c'^g$	0	0	0	0	0	
	PF	25	25	25	25	25	
	$\mathbf{th}_s$	0	0	0	0	0	
	$\mathbf{th}_c$	0	0	0	0	0	

The tabular values show the simulated loss (S.L.) for all parameters. The color code is based on Table 2, and the nominal value of parameters is defined in Table 3. Parameters printed in bold styles are solely used in damage simulation and are not estimated in the model updating process.

Table 5: The vehicle speed, entrance time, and the relative initial errors for vehicular loads for D03.

	Vehicle ID													
	1	2	3	4	5	6	7	8	9	10	11	12	13	14
Speed (m/ sec)	28.80	28.34	28.35	28.35	28.35	28.35	25.10	27.00	27.00	27.00	27.00	27.00	27.00	27.00
Entrance time (sec)	0.01	3.2	6.39	9.53	12.66	15.79	18.96	0.01	3.18	6.33	9.53	12.69	15.78	18.9
RIE for vehicular loads (%)	19.3	10.23	2.45	15.0	4.56	14.4	8.2	0.1	16.2	25.8	17.6	−11	4.0	1.0

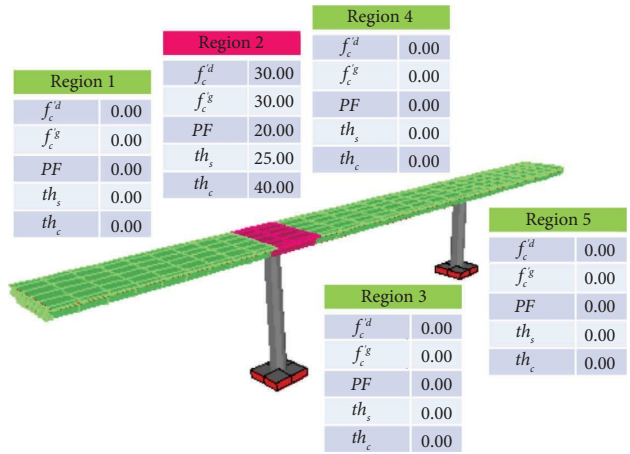

Figure 11: True damage state for damage scenario D03. The tabulated values show the simulated loss (S.L.), see equation (20) and Table 4.

The initial estimates of the prestressing force in all regions are 30% less than their nominal values, resulting in −30% to −13% relative initial error (RIE, see equation (22)), and the initial estimates of the effective compressive strength of top slab and girders in all regions are 35% less than their corresponding nominal values, resulting in −35% to −7% RIE. In this case, 14 vehicles passed the bridge over the 20 second period of measurement. The RIE for vehicular loads are listed in Table 5 and are assigned randomly. Vehicles 1 to 7 enter the first lane of traffic, and vehicles 8 to 14 enter the other lane. The corresponding speed and the entrance time of each vehicle are listed in this table.

The updating process of the posterior estimate of model parameters (normalized by their corresponding true values) for damage scenario D03 are shown in Figure 12. In this figure, the horizontal axis represents the total number of estimation iterations, and the vertical dashed lines show the transition point from one estimation window to the next. As can be seen in this figure, all the model parameters are iteratively updated from the initial to their final estimates. The final estimates of $f_c'^g$ in all regions are well converged to the corresponding true values. The Relative estimation error (REE) for each parameter is defined as

$$\text{Relative Estimation Error (REE) (\%)} = \left(\frac{\text{Final estimate}}{\text{True value}} - 1\right) \times 100. \tag{22}$$

The maximum REE for $f_c'^g$ is 5% and is associated with region 1. The localized damage in region 2 is well estimated with only −1% REE. Following Figure 12(b), the final estimate of $f_c'^d$ in regions 1, 3, 4, and 5 are converged to their corresponding true values with maximum REE of 6% in region 5. However, $f_c'^d$ in region 2 is not converged to its true value with an apparent REE of −40%. The reason for this discrepancy is that in this region, in addition to concrete degradation, concrete delamination and steel reinforcement corrosion are also implicitly estimated through the effective compressive strength of top slab. So, the excessive REE in this parameter incorporates concrete delamination and steel reinforcement corrosion and is so called "apparent" REE. Although damage and its location are correctly detected, these three types of damage are not distinguishable in practice. Due to this reason, further investigations may be needed to attribute concrete degradation, delamination, corrosion, or a combination of them to an identified damage state. As can be seen in Figure 12(c), although the parameters PF are iteratively updated and converged through the model updating process, their corresponding REE is between −6% and 8%, which is higher than other parameters. This inaccuracy in estimating the prestressing forces is due to their weak identifiability as mentioned earlier.

To better understand the estimation results, Figure 13 compares the nominal values, true values, and initial and final estimates of model parameters for damage scenario D03 in all five regions. This figure clearly shows that regardless of the level of RIE in the model parameters, the final estimates are close to the true values. As already mentioned,

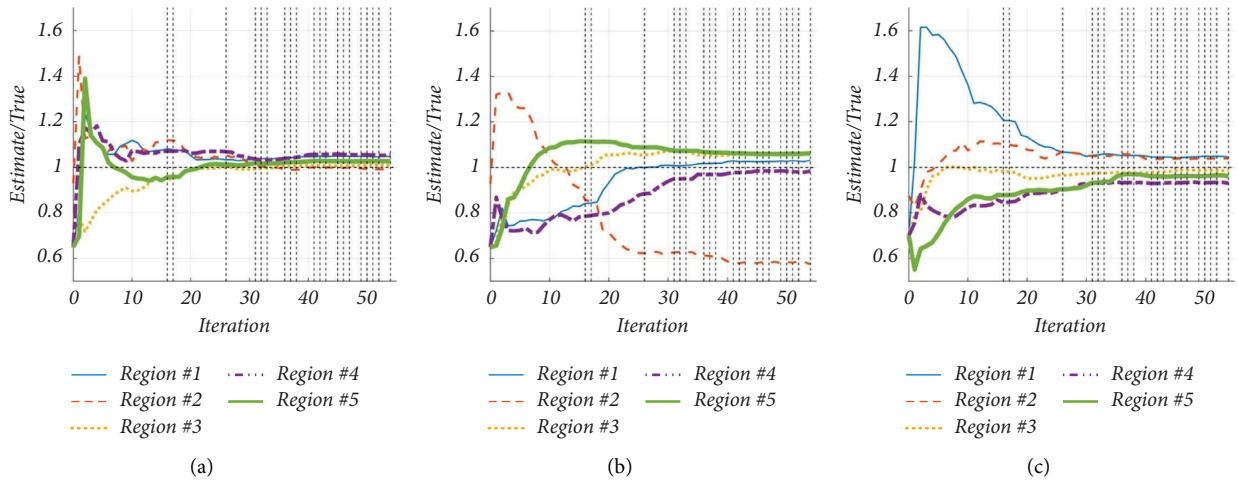

FIGURE 12: Updating process of the posterior estimate of model parameters using measurement data obtained from damage scenario D03: (a) effective compressive strength of girders ($f_c^{'g}$), (b) effective compressive strength of top slab ($f_c^{'d}$), and (c) prestressing force (PF).

the difference between final estimates and true values of $f_c^{'d}$ at region 2 is due to the fact that this parameter absorbs both the delamination and rebar corrosion effects.

Figure 14 compares the true values and initial and final estimates of vehicular loads for damage scenario D03. The figure shows that all vehicular loads are correctly estimated regardless of their corresponding RIE. The maximum absolute REE is for vehicle 1, which is less than 1%. These results demonstrate the capability and efficiency of the proposed approach to estimate vehicular loads. In this study, the RIE values for vehicular loads are selected randomly (using uniform distribution function) between +35% and −35%.

Finally, the true and estimated damage state of the bridge can be compared using Figures 11 and 15. The estimated loss for each model parameter is tabulated in Figure 15 and is defined as

$$\text{Estimated Loss (E.L.) (\%)} = \left(1 - \frac{\text{Final estimate}}{\text{Nominal value}}\right) \times 100 \geq 0. \tag{23}$$

According to Figure 15, the damage state of regions 1, 2, 3 and 5 are identified correctly. Region 4 with no damage, is incorrectly identified with minor damaged region due the estimated loss in PF.

For the sake of brevity, the final results and a comparison between the true and estimated damage state of the bridge for all 10 damage scenarios are shown in Table 6. The tabulated values in this table are the REE for each estimation parameter at each region, and the corresponding RIE is shown in parentheses. The table also compares the color-coded true damage estimates with the estimated ones. As can be seen in this table, the localized minor degradation in D01 is well identified. However, in region 4, although the model parameters $f_c^{'g}$ and PF are correctly identified, the slight inaccuracy in identified $f_c^{'d}$ results in estimation of a minor damage state in this region. The inaccuracy in estimation of $f_c^{'d}$ at region 4 was expected due to the small entropy gain of this parameter as observed in the identifiability assessment, see parameter 14 in Figure 9(a). In D02, regions 4 and 5, which are undamaged, are identified with minor damage. The incorrect damage identification in both regions 4 and 5 are due to inaccurate estimation of the parameter PF, which was expected due to the weak identifiability, see parameters 1 to 5 in Figure 9(a). In D02, reinforcement corrosion and top slab delamination in region 2 are implicitly estimated through the parameter $f_c^{'d}$, and the final damage state of this region is estimated correctly. D04 resembles D01, but with distributed (instead of localized) damage along all regions. As can be seen, the damage state at all regions is identified correctly. In D05, the distributed mild damage state of the bridge is estimated successfully along the bridge. Damage scenario D06 is the most challenging damage scenario as it includes various damage mechanisms in all regions. In this scenario, all five regions experience minor concrete degradation and delamination, as well as mild top slab reinforcement and tendon corrosion resulting in mild damage state in all regions. The model updating process incorrectly identifies region 4 with severe damage while the other regions are identified correctly with mild damage. The inaccuracy in damage state identification of region 4 is due to inaccurate estimation of parameter $f_c^{'d}$, which was expected due to its weak identifiability. Damage scenario D07 only includes localized top slab concrete delamination and reinforcement corrosion, which are expected to implicitly reflect on the $f_c^{'d}$ estimate. This damage scenario directly examines the proposal to implicitly estimate these damage mechanisms through a reduction in $f_c^{'d}$. As can be seen in Table 6, the successful bridge damage state identification

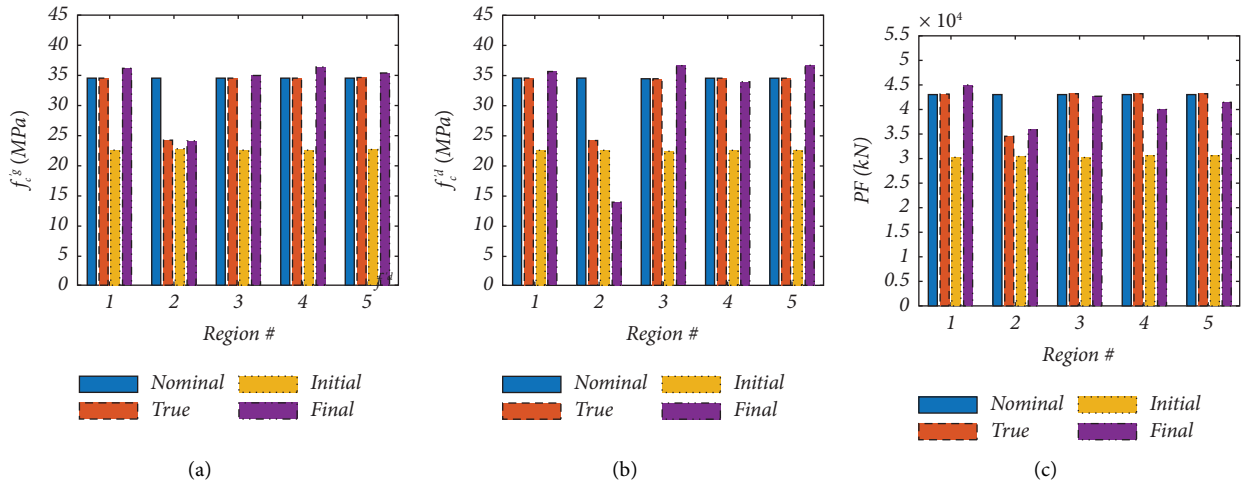

FIGURE 13: Comparisons of the nominal and true values and initial and final estimates of model parameters for damage scenario D03: (a) effective compressive strength of girders ($f_c^{'g}$), (b) effective compressive strength of top slab ($f_c^{'d}$), and (c) prestressing force (PF).

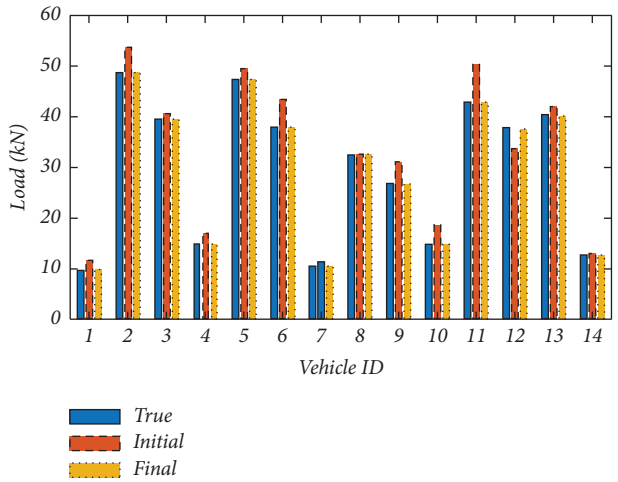

FIGURE 14: Comparisons of the true values and initial and final estimates of vehicular loads using measurement data obtained from damage scenario D03.

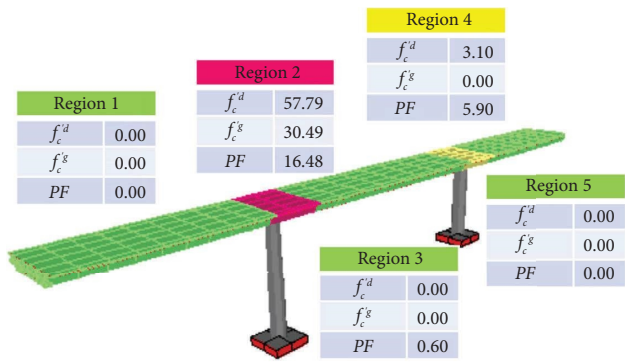

FIGURE 15: Estimated damage state for damage scenario D03. The tabulated values show the estimated loss (E.L.) (see equation (23)) and can be compared with the simulated loss (S.L.) in Figure 11.

Table 6: Relative initial and estimation error of model parameters, and the true and estimated damage state of bridge.

Damage scenario I.D.	Parameter I.D.	REE (RIE) Region # 1	2	3	4	5	True damage state	Estimated damage state
D01	$f_c'^d$	-2 (-20)	5 (-11)	-2 (-20)	-6 (-20)	0 (-20)		
	$f_c'^g$	0 (-20)	-2 (-11)	0 (-20)	1 (-20)	0 (-20)		
	PF	3 (10)	1 (10)	2 (10)	-1 (10)	-1 (10)		
D02	$f_c'^d$	3 (-25)	-33* (13)	6 (-30)	0 (-20)	5 (20)	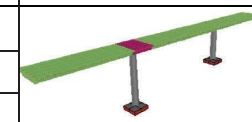	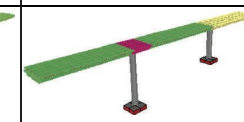
	$f_c'^g$	4 (10)	1 (29)	1 (-30)	4 (-5)	2 (-5)		
	PF	0 (10)	1 (0)	-1 (-5)	-6 (-5)	-5 (-10)		
D03	$f_c'^d$	1 (-35)	-40* (-7)	5 (-35)	-3 (-35)	6 (-35)	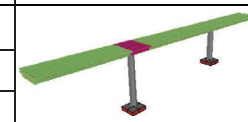	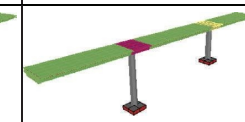
	$f_c'^g$	5 (-35)	-1 (-7)	1 (-35)	4 (-35)	3 (-35)		
	PF	8 (-30)	4 (-13)	-2 (-30)	-6 (-30)	-2 (-30)		
D04	$f_c'^d$	0 (-11)	2 (-16)	-1 (-11)	-2 (-11)	0 (-11)	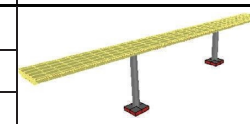	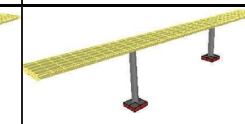
	$f_c'^g$	0 (22)	-1 (16)	0 (16)	2 (16)	0 (22)		
	PF	6 (-20)	1 (-20)	1 (-20)	-6 (-20)	3 (-20)		
D05	$f_c'^d$	0 (13)	0 (13)	0 (6)	0 (13)	0 (13)		
	$f_c'^g$	0 (6)	0 (13)	0 (6)	0 (6)	0 (13)		
	PF	0 (0)	2 (0)	0 (-5)	1 (6)	0 (0)		
D06	$f_c'^d$	-16* (-16)	-5* (-11)	-9* (-16)	-25* (-11)	-12* (-16)	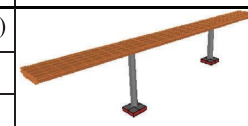	
	$f_c'^g$	11 (-16)	0 (-11)	3 (-16)	2 (-11)	10 (-16)		
	PF	11 (-13)	-1 (-7)	-2 (-13)	4 (-7)	-4 (-13)		
D07	$f_c'^d$	1 (-10)	-12* (-10)	3 (-10)	-2 (-10)	3 (-10)	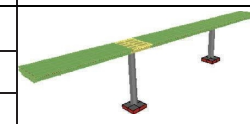	
	$f_c'^g$	1 (10)	2 (10)	0 (10)	3 (10)	1 (10)		
	PF	-2 (-10)	-5 (-10)	-1 (-10)	-5 (-10)	-2 (-10)		
D08	$f_c'^d$	1 (-20)	-49* (7)	8 (-20)	-4 (-20)	8 (-20)	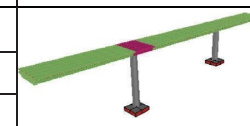	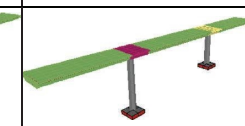
	$f_c'^g$	7 (-20)	0 (-20)	1 (-20)	4 (-20)	4 (-20)		
	PF	2 (-10)	3 (-10)	-1 (-10)	-5 (-10)	-3 (-10)		
D09	$f_c'^d$	0 (-20)	-1 (-20)	0 (-20)	1 (-20)	0 (-20)	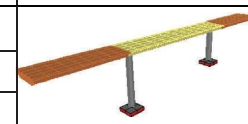	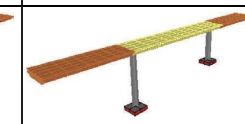
	$f_c'^g$	0 (-20)	0 (-20)	0 (-20)	0 (-20)	0 (-20)		
	PF	0 (7)	2 (-6)	0 (-6)	-1 (-6)	1 (7)		
D10	$f_c'^d$	0 (-20)	0 (-20)	0 (-20)	-1 (-20)	-1 (-20)	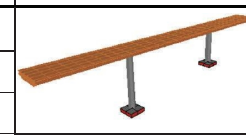	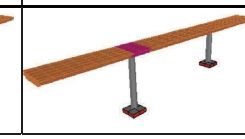
	$f_c'^g$	0 (-20)	1 (-20)	0 (-20)	0 (-20)	1 (-20)		
	PF	2 (20)	-8 (20)	6 (20)	8 (20)	-6 (20)		

*Apparent relative estimation error incorporating the implicit effect of other damage mechanisms. REE: relative estimation error based on equation (23) and RIE: relative initial error based on equation (21).

in this scenario shows the acceptable outcome of the approach. Damage scenario D08 resembles damage scenario D07; however, in addition to the top slab reinforcement corrosion and delamination in region 2, in this scenario severe concrete degradation is also expected to be estimated through $f_c'^d$. The damage state of all regions is identified correctly except region 4 due to PF weak identifiability. Finally, damage scenarios D09 and D10 represent nonuniform and uniform loss of prestressing force loss in all five regions. In these two scenarios, the damage state at all regions except region 2 in D10 is estimated correctly. The corresponding incorrect damage identifications are due to slight inaccuracy in PF estimation.

Table 7: Relative initial and estimation error of vehicular load parameters.

Error	D01	D02	D03	D04	D05	D06	D07	D08	D09	D010
Extremum RIE (%)	−33	−35	26	29	−32	−27	−33	−33	−28	−31
Extremum REE (%)	0	0	1	0	0	1	0	−2	−1	0

Table 7 lists the extremum RIE and REE of vehicular loads in all the 10 studied damage scenarios. This table shows that the vehicular loads are estimated correctly regardless of the initial estimation error. While the RIE of vehicular loads reach as high as 35%, all the vehicular loads are estimated with ±2% REE.

In summary, the relatively strong correlation between the final estimates and true values for model and vehicular load parameters verify the damage identification potential for the proposed approach. In all the 10 studied damage scenarios, damage states for 86% of regions are estimated correctly. For the remaining regions, damage states are all expressed conservatively, meaning that damage in no region is underestimated.

6. Conclusions

This paper introduced a novel formulation for a time-domain Bayesian finite element (FE) model updating technique to jointly estimate the model parameters and vehicular loads using the measured dynamic responses of the bridge and vehicle locations. For this purpose, a rolling estimation window scheme was used where the time-domain data was divided into estimation windows, each of which started from the first time step. At each estimation window, the joint probability density function (PDF) of the model parameters and vehicular loads was updated iteratively and the posterior mean vector and covariance matrix were estimated, which were then transferred to the next estimation window and used as prior information. The final estimates of the model parameters were used to infer the location, mechanism, and extent of damage through the length of the bridge. The proposed approach can offer a cost-effective complementary screening method for other damage identification and condition assessment approaches—e.g., nondestructive evaluation (NDE) methods—to guide their targeted application and overcome the gaps in the current engineering practice.

The efficacy of the proposed Bayesian FE model updating technique to identify various damage scenarios were tested using a series of numerically simulated verification studies. The studies were performed on a prestressed concrete box-girder bridge model in OpenSees under random traffic loads. Concrete degradation, delamination, steel corrosion, and loss of prestressing force were considered as possible damage mechanisms across five regions along the bridge. Ten (10) different scenarios, including *minor localized* to *severe distributed* damage scenarios were considered. An identifiability assessment was performed to determine the likely identifiable model parameters and the most informative measurement channels. The damage states at bridge regions were estimated accurately in 86% of cases and with minor errors in other cases. Conservatively, none of the damages in any of the five regions was underestimated. The vehicular loads were estimated with less than 1% error. The results of the Bayesian FE model updating technique and its demonstrated success in damage identification verified the developed formulation and were a positive step forward towards seeking and achieving the validation through field tests.

Data Availability

All data are available from the corresponding author upon reasonable request.

Conflicts of Interest

The authors declare that there are no conflicts of interest regarding the publication of this paper.

Acknowledgments

This project was funded through the United States Department of Transportation Small Business Innovative Research (SBIR) program Phase I (Contract #6913G618P800109) and Phase II (Contract #6913G619C100048). The financial support is gratefully acknowledged. The project resulted from the collaboration between S.C. Solutions, Inc., the leading small business, the University of California Los Angeles, and the University of Nevada, Reno. Opinions and findings in this study are those of the authors and do not necessarily reflect the views of the sponsor.

References

[1] ASCE, *Infrastructure Report Card*, ASCE, Reston, DC, USA, 2017.

[2] S. Kashif Ur Rehman, Z. Ibrahim, S. A. Memon, and M. Jameel, "Nondestructive test methods for concrete bridges: a review," *Construction and Building Materials*, vol. 107, pp. 58–86, 2016.

[3] B. A. Graybeal, B. M. Phares, D. D. Rolander, M. Moore, and G. Washer, "Visual inspection of highway bridges," *Journal of Nondestructive Evaluation*, vol. 21, no. 3, pp. 67–83, 2002.

[4] M. Moore, B. Phares, B. Graybeal, D. Rolander, and G. Washer, "Reliability of visual inspection for highway bridges volume I: final report," 2001, https://www.fhwa.dot.gov/publications/research/nde/01020.cfm.

[5] A. Nair and C. S. Cai, "Acoustic emission monitoring of bridges: review and case studies," *Engineering Structures*, vol. 32, no. 6, pp. 1704–1714, 2010.

[6] D. M. McCann and M. C. Forde, "Review of NDT methods in the assessment of concrete and masonry structures," *NDT & E International*, vol. 34, no. 2, pp. 71–84, 2001.

[7] M. Scott, A. Rezaizadeh, A. Delahaza et al., "A comparison of nondestructive evaluation methods for bridge deck assessment," *NDT and E International*, vol. 36, no. 4, pp. 245–255, 2003.

[8] U.S. Department of Transportation and Federal Highway Administration, "Bridge condition by functional classification

area 2019," 2019, https://www.fhwa.dot.gov/bridge/nbi/no10/fcarea19.cfm.

[9] S. Dorafshan and H. Azari, "Evaluation of bridge decks with overlays using impact echo, a deep learning approach," *Automation in Construction*, vol. 113, Article ID 103133, 2020.

[10] S. Dorafshan and H. Azari, "Deep learning models for bridge deck evaluation using impact echo," *Construction and Building Materials*, vol. 263, Article ID 120109, 2020.

[11] M. L. Fugate, H. Sohn, and C. R. Farrar, "Vibration-based damage detection using statistical process control," *Mechanical Systems and Signal Processing*, vol. 15, no. 4, pp. 707–721, 2001.

[12] C. Farrar and P. Cornwell, "Structural health monitoring studies of the alamosa canyon and i-40 bridges," LA-13635-MS TRN: AH200036%%36, OSTI.Gov, CA, USA, 2000.

[13] W. Fan and P. Qiao, "Vibration-based damage identification methods: a review and comparative study," *Structural Health Monitoring*, vol. 10, no. 1, pp. 83–111, 2011.

[14] M. Friswell and J. E. Mottershead, *Finite Element Model Updating in Structural Dynamic*, Springer International Publishing, Berlin, Germany, 1995.

[15] F. Abazarsa, F. Nateghi, S. F. Ghahari, and E. Taciroglu, "Extended blind modal identification technique for non-stationary excitations and its verification and validation," *Journal of Engineering Mechanics*, vol. 142, no. 2, 2016.

[16] S. F. Ghahari, F. Abazarsa, O. Avci, M. Celebi, and E. Taciroglu, "Blind identification of the Millikan Library from earthquake data considering soil–structure interaction," *Structural Control and Health Monitoring*, vol. 23, no. 4, pp. 684–706, 2016.

[17] S. F. Ghahari, F. Abazarsa, M. A. Ghannad, M. Celebi, and E. Taciroglu, "Blind modal identification of structures from spatially sparse seismic response signals," *Structural Control and Health Monitoring*, vol. 21, 2013.

[18] F. Zareian, P. Kaviani, and E. Taciroglu, "Multiphase performance assessment of structural response to seismic excitations," *Journal of Structural Engineering*, vol. 141, Article ID 04015041, pp. 1–10, 2015.

[19] R. Omrani, B. Mobasher, X. Liang et al., "Guidelines for nonlinear seismic analysis of ordinary bridges: version 2.0," University of California, Berkeley, CA, USA, CA15-2266, 2015.

[20] H. Ebrahimian, R. Astroza, J. P. Conte, and R. A. De Callafon, "Nonlinear finite element model updating for damage identification of civil structures using batch Bayesian estimation," *Mechanical Systems and Signal Processing*, vol. 84, pp. 194–222, 2017.

[21] H. Ebrahimian, R. Astroza, J. P. Conte, and C. Papadimitriou, "Bayesian optimal estimation for output-only nonlinear system and damage identification of civil structures," *Structural Control and Health Monitoring*, vol. 25, no. 4, pp. e2128–e2132, 2018.

[22] M. Hoshiya and E. Saito, "Structural identification by extended Kalman filter," *Journal of Engineering Mechanics*, vol. 110, pp. 1757–1770, 1985.

[23] C. G. Koh, L. M. See, and T. Balendra, "Estimation of structural parameters in time domain: a substructure approach," *Earthquake Engineering & Structural Dynamics*, vol. 20, no. 8, pp. 787–801, 1991.

[24] J. Lin and Y. Zhang, "Nonlinear structural identification using extended Kalman filter," *Computers & Structures*, vol. 52, no. 4, pp. 757–764, 1994.

[25] R. Omrani, R. E. Hudson, and E. Taciroglu, "Parametric identification of nondegrading hysteresis in a laterally and torsionally coupled building using an unscented kalman filter," *Journal of Engineering Mechanics*, vol. 139, no. 4, pp. 452–468, 2013.

[26] M. Lee and Y. Liu, "Input load identification of nonlinear tower structural system using intelligent inverse estimation algorithm," *Procedia Engineering*, vol. 79, pp. 540–549, 2014.

[27] A. Al-hussein and A. Haldar, "Novel Unscented Kalman filter for health assessment of structural systems with unknown input," *Journal of Engineering Mechanics*, vol. 141, pp. 1–13, 2015.

[28] S. Eftekhar Azam, E. Chatzi, C. Papadimitriou, and A. Smyth, "Experimental validation of the Kalman-type filters for online and real-time state and input estimation," *Journal of Vibration and Control*, vol. 23, no. 15, pp. 2494–2519, 2017.

[29] S. Eftekhar Azam, E. Chatzi, and C. Papadimitriou, "A dual Kalman filter approach for state estimation via output-only acceleration measurements," *Mechanical Systems and Signal Processing*, vol. 60-61, pp. 866–886, 2015.

[30] E. Yu, E. Taciroglu, and J. W. Wallace, "Parameter identification of framed structures using an improved finite element model-updating method — Part I: formulation and verification," *Earthquake Engineering & Structural Dynamics*, vol. 36, no. 5, pp. 619–639, 2007.

[31] M. Song, R. Astroza, H. Ebrahimian, B. Moaveni, and C. Papadimitriou, "Adaptive Kalman filters for nonlinear finite element model updating," *Mechanical Systems and Signal Processing*, vol. 143, Article ID 106837, 2020.

[32] H. Ebrahimian, M. Kohler, A. Massari, and D. Asimaki, "Parametric estimation of dispersive viscoelastic layered media with application to structural health monitoring," *Soil Dynamics and Earthquake Engineering*, vol. 105, pp. 204–223, 2018.

[33] H. Ebrahimian, R. Astroza, J. P. Conte, and C. Papadimitriou, "A nonlinear model inversion method for joint system parameter, noise, and input identification of civil structures," *Procedia Engineering*, vol. 199, pp. 924–929, 2017.

[34] F. Ghahari, N. Malekghaini, H. Ebrahimian, and E. Taciroglu, "Bridge digital twinning using an output-only Bayesian model updating method and recorded seismic measurements," *Sensors*, vol. 22, no. 3, p. 1278, 2022.

[35] N. Shirzad-Ghaleroudkhani, M. Mahsuli, S. F. Ghahari, and E. Taciroglu, "Bayesian identification of soil-foundation stiffness of building structures," *Structural Control and Health Monitoring*, vol. 25, no. 3, pp. e2090–e2108, 2018.

[36] M. S. Nabiyan, F. Khoshnoudian, B. Moaveni, and H. Ebrahimian, "Mechanics-based model updating for identification and virtual sensing of an offshore wind turbine using sparse measurements," *Structural Control and Health Monitoring*, vol. 28, no. 2, 2021.

[37] L. Ge, D. Dan, K. Y. Koo, and Y. Chen, "Long-term monitoring system for full-bridge traffic load distribution on long-span bridges," *Engineering Archive*, 2022.

[38] M. Rezaei, M. Azarmi, F. Mohammad, and P. Mir, "Traffic-Net: 3D traffic monitoring using a single camera," 2021, https://arxiv.org/abs/2109.09165.

[39] J. Redmon and A. Farhadi, "YOLOv3: an incremental improvement," 2018, https://arxiv.org/abs/1804.02767.

[40] N. Wojke, A. Bewley, and D. Paulus, "Simple online and realtime tracking with a deep association metric," in *Proceedings of the 2017 IEEE International Conference on Image Processing (ICIP)*, Beijing, China, September, 2017.

[41] S. F. Ghahari, H. Ebrahimian, and E. Taciroglu, "Investigation of the spatial variability of seismic input motions for CSMIP-instrumented bridges during the 2014 South Napa

earthquake—the case of Golden Gate Bridge," in *17th SMIP Semin. Util. Strong Motion Data*Califonria Geological Survey, Berkeley, CA, USA, 2017.
[42] D. Simon, *Optimal State Estimation*, John Wiley & Sons, Inc, Hoboken, NJ, USA, 1994.
[43] J. L. Beck, "Bayesian system identification based on probability logic," *Structural Control and Health Monitoring*, vol. 17, no. 7, pp. 825–847, 2010.
[44] M. Muto and J. L. Beck, "Bayesian updating and model class selection for hysteretic structural models using stochastic simulation," *Journal of Vibration and Control*, vol. 14, no. 1-2, pp. 7–34, 2008.
[45] K. V. Yuen, J. L. Beck, and L. S. Katafygiotis, "Unified probabilistic approach for model updating and damage detection," *Journal of Applied Mechanics*, vol. 73, no. 4, pp. 555–564, 2006.
[46] K. V. Yuen and S. C. Kuok, "Bayesian methods for updating dynamic models," *Applied Mechanics Reviews*, vol. 64, no. 1, 2011.
[47] ACI Committee 365, *Report on Service Life Prediction*, Farmington Hills, Oakland, MI, USA, 2017.
[48] ACI Committee 201, *Guide to Durable Concrete*, Farmington Hills, Oakland, MI, USA, 2008.
[49] N. Gucunski, A. Imani, F. Romero et al., *Nondestructive Testing to Identify concrete Bridge Deck Deterioration*, Transportation Research Board, Washington, DC, USA, 2013.
[50] K. Suda, S. Misra, and K. Motohashi, "Corrosion products of reinforcing bars embedded in concrete," *Corrosion Science*, vol. 35, no. 5-8, pp. 1543–1549, 1993.
[51] W. Zhu, "Effect of corrosion on the mechanical properties of the corroded reinforcement and the residual structural performance of the corroded beams," 2015, https://tel.archives-ouvertes.fr/tel-01222175/document.
[52] S. A. A. K. Azad and S. A. Azher, "Residual strength of corrosion-damaged reinforced concrete beams," *ACI Materials Journal*, vol. 104, pp. 40–47, 2007.
[53] Ministry of Public Works and Transport, *Bridge Inspection Manual*, Ministry of Public Works and Transport, Oakdale, CA, USA, 2016.
[54] I. Fernandez, M. F. Herrador, A. R. Marí, and J. M. Bairán, "Structural effects of steel reinforcement corrosion on statically indeterminate reinforced concrete members," *Materials and Structures*, vol. 49, no. 12, pp. 4959–4973, 2016.
[55] M. Ismail, B. Muhammad, and M. E. G. Ismail, "Compressive strength loss and reinforcement degradations of reinforced concrete structure due to long-term exposure," *Construction and Building Materials*, vol. 24, no. 6, pp. 898–902, 2010.
[56] B. Li, L. Cai, K. Wang, and Y. Zhang, "Prediction of the residual strength for durability failure of concrete structure in acidic environments," *Journal of Wuhan University of Technology-Materials Science Edition*, vol. 31, no. 2, pp. 340–344, 2016.
[57] A. M. Diab, H. E. Elyamany, A. E. M. Abd Elmoaty, and A. H. Shalan, "Prediction of concrete compressive strength due to long term sulfate attack using neural network," *Alexandria Engineering Journal*, vol. 53, no. 3, pp. 627–642, 2014.
[58] R. Rashetnia, F. Ghasemzadeh, M. Hallaji, and M. Pour-Ghaz, "Quantifying prestressing force loss due to corrosion from dynamic structural response," *Journal of Sound and Vibration*, vol. 433, pp. 129–137, 2018.
[59] F. McKenna, "OpenSees: a framework for earthquake engineering simulation," *Computer Science and Engineering*, vol. 13, no. 4, pp. 58–66, 2011.
[60] H. Ebrahimian, R. Astroza, J. P. Conte, and R. R. Bitmead, "Information-theoretic approach for identifiability assessment of nonlinear structural finite-element models," *Journal of Engineering Mechanics*, vol. 145, no. 7, pp. 1–14, 2019.
[61] MathWorks, "Matlab R2019a," 2019, https://www.mathworks.com/help/matlab/release-notes-R2019a.html.
[62] X. Lu, L. Xie, H. Guan, Y. Huang, and X. Lu, "A shear wall element for nonlinear seismic analysis of super-tall buildings using OpenSees," *Finite Elements in Analysis and Design*, vol. 98, pp. 14–25, 2015.